Journal of Asian Earth Sciences 127 (2016) 76–90

Contents lists available at ScienceDirect

Journal of Asian Earth Sciences

journal homepage: www.elsevier.com/locate/jseaes

Full length Article

Magma-derived CO_2 emissions in the Tengchong volcanic field, SE Tibet: Implications for deep carbon cycle at intra-continent subduction zone

Maoliang Zhang [a,b], Zhengfu Guo [a,*], Yuji Sano [c], Lihong Zhang [a], Yutao Sun [a,b], Zhihui Cheng [a,b], Tsanyao Frank Yang [d]

[a] Key Laboratory of Cenozoic Geology and Environment, Institute of Geology and Geophysics, Chinese Academy of Sciences, Beijing 100029, China
[b] University of Chinese Academy of Sciences, Beijing 100049, China
[c] Atmosphere and Ocean Research Institute, University of Tokyo, Kashiwa-noha, Chiba 277-8564, Japan
[d] Department of Geosciences, National Taiwan University, Taipei 10699, Taiwan

ARTICLE INFO

Article history:
Received 17 March 2016
Received in revised form 10 June 2016
Accepted 13 June 2016
Available online 14 June 2016

Keywords:
Soil CO_2 flux
Deep carbon cycle
Gas geochemistry
Continental subduction zone
SE Tibet

ABSTRACT

Active volcanoes at oceanic subduction zone have long been regard as important pathways for deep carbon degassed from Earth's interior, whereas those at continental subduction zone remain poorly constrained. Large-scale active volcanoes, together with significant modern hydrothermal activities, are widely distributed in the Tengchong volcanic field (TVF) on convergent boundary between the Indian and Eurasian plates. They provide an important opportunity for studying deep carbon cycle at the ongoing intra-continent subduction zone. Soil microseepage survey based on accumulation chamber method reveals an average soil CO_2 flux of ca. 280 g m^{-2} d^{-1} in wet season for the Rehai geothermal park (RGP). Combined with average soil CO_2 flux in dry season (ca. 875 g m^{-2} d^{-1}), total soil CO_2 output of the RGP and adjacent region (ca. 3 km^2) would be about 6.30×10^5 t a^{-1}. Additionally, we conclude that total flux of outgassing CO_2 from the TVF would range in $(4.48–7.05) \times 10^6$ t a^{-1}, if CO_2 fluxes from hot springs and soil in literature are taken into account. Both hot spring and soil gases from the TVF exhibit enrichment in CO_2 (>85%) and remarkable contribution from mantle components, as indicated by their elevated $^3He/^4He$ ratios (1.85–5.30 R_A) and $\delta^{13}C$-CO_2 values (−9.00‰ to −2.07‰). He-C isotope coupling model suggests involvement of recycled organic metasediments and limestones from subducted Indian continental lithosphere in formation of the enriched mantle wedge (EMW), which has been recognized as source region of the TVF parental magmas. Contamination by crustal limestone is the first-order control on variations in He-CO_2 systematics of volatiles released by the EMW-derived melts. Depleted mantle and recycled crustal materials from subducted Indian continental lithosphere contribute about 45–85% of the total carbon inventory, while the rest carbon (about 15–55%) is accounted by limestones in continental crust. As indicated by origin and evolution of the TVF volatiles, mantle-derived magmas at continental subduction zone can act as important triggers for liberation of carbon stored in crustal carbonate rocks, which has the potential to be a complement to volatile recycling mechanism at subduction zones. Variations in He-Nd-Sr isotopes of magmas and volatiles from different types of plate boundaries suggest higher amounts of recycled materials for mantle wedge enrichment of continental subduction zone relative to that of oceanic subduction zone.

1. Introduction

The India-Asia continent collision at 55–50 Ma (e.g., Najman et al., 2010; Bouilhol et al., 2013; Zhu et al., 2015; Ding et al., 2016), accompanied by subsequent underthrusting of the Indian continental lithosphere beneath the Asian continent (e.g., DeCelles et al., 2011; Capitanio and Replumaz, 2013; Wang et al., 2014; Shi et al., 2015), led to formation of the Tibetan Plateau with an average elevation about 5000 m above sea level (Fielding et al., 1994), which has been widely invoked as critical geological event responsible for global cooling, central Asian aridification and East Asian monsoon intensification in the Cenozoic (e.g., Guo et al., 2002; Dupont-Nivet et al., 2007; Clift et al., 2008; Wu et al., 2012; Zheng et al., 2015). Nevertheless, significant debates still exist on possible links between global climate change and the India-Asia continent collision (Kerrick and Caldeira, 1999;

* Corresponding author at: No. 19, Beitucheng Western Road, Chaoyang District, Beijing 100029, China.
E-mail address: zfguo@mail.iggcas.ac.cn (Z. Guo).

http://dx.doi.org/10.1016/j.jseaes.2016.06.009
1367-9120/

Willenbring et al., 2013), because silicate weathering in response to plateau uplift sequesters carbon (Raymo and Ruddiman, 1992; Dosseto et al., 2015), whereas syn-collisional volcanism (e.g. Mo et al., 2008; Niu et al., 2013; Zhu et al., 2015), post-collisional volcanism (Guo et al., 2006, 2007, 2013, 2014a, 2015a,b; L. Zhang et al., 2015), subduction zone metamorphism (Kerrick and Connolly, 2001; Cook-Kollars et al., 2014) and modern hydrothermal activities (Guo et al., 2014b; Zhang et al., 2014) release carbon. Additionally, chemical geodynamics of volatile recycling at mid-ocean ridge (MOR; Graham, 2002; Stagno et al., 2013; Burley and Katz, 2015; Kagoshima et al., 2015) and oceanic subduction zone (OSZ; Sano and Williams, 1996; Lee and Lackey, 2015; Kelemen and Manning, 2015; Zellmer et al., 2015) have been well established, while little attention has been paid to volatile recycling at continental subduction zone (CSZ) and continental collision zone (CCZ), which highlights the importance of investigating flux and origin of volatiles (e.g., CO_2) from convergent boundaries between continental plates.

Active volcanoes at the India-Asia continental subduction zone, which only exist in the Tengchong volcanic field (TVF; e.g., Zou et al., 2010, 2014; Guo et al., 2015a), SE Tibet, are excellent windows for insights into deep carbon flux and genesis of volatiles released by continental subduction-related volcanism (Fig. 1). The TVF is characterized by both large-scale Holocene volcanic eruptions [including the Dayingshan active volcano, which erupted at CE 1609 as described by Chinese geographer Xu Xiake (1587–1641) of the Ming Dynasty; Huangfu and Jiang, 2000] and significant hydrothermal activities (Xu et al., 2004; Shangguan et al., 2005; Guo and Wang, 2012). Recent geochemical studies (e.g., Guo et al., 2015a) have recognized the Indian continent-derived components in mantle source region of the Late Cenozoic high-K calc-alkaline volcanic rocks in the TVF. High-resolution seismic tomographic evidence reveals eastward underthrusting of the Indian continental lithosphere into asthenospheric mantle beneath the TVF (Huang and Zhao, 2006; Lei et al., 2013; Lei and Zhao, 2016). Moreover, low-velocity anomaly beneath active volcanoes provides evidence for the existence of crustal magma chamber (e.g., Xu et al., 2012; Yang et al., 2013), indicating that the TVF is an ideal laboratory for studying deep carbon cycle and magma-derived CO_2 emissions at the India-Asia continental subduction zone.

In this study, we report soil CO_2 flux of the Rehai geothermal park (RGP) using accumulation chamber method, and estimate total magma-derived CO_2 flux of the whole TVF based on previous studies (Cheng et al., 2012, 2014). Additionally, new data of elemental and He-C isotopic compositions are reported for hot spring gases, aiming to constrain origin and evolution of the TVF

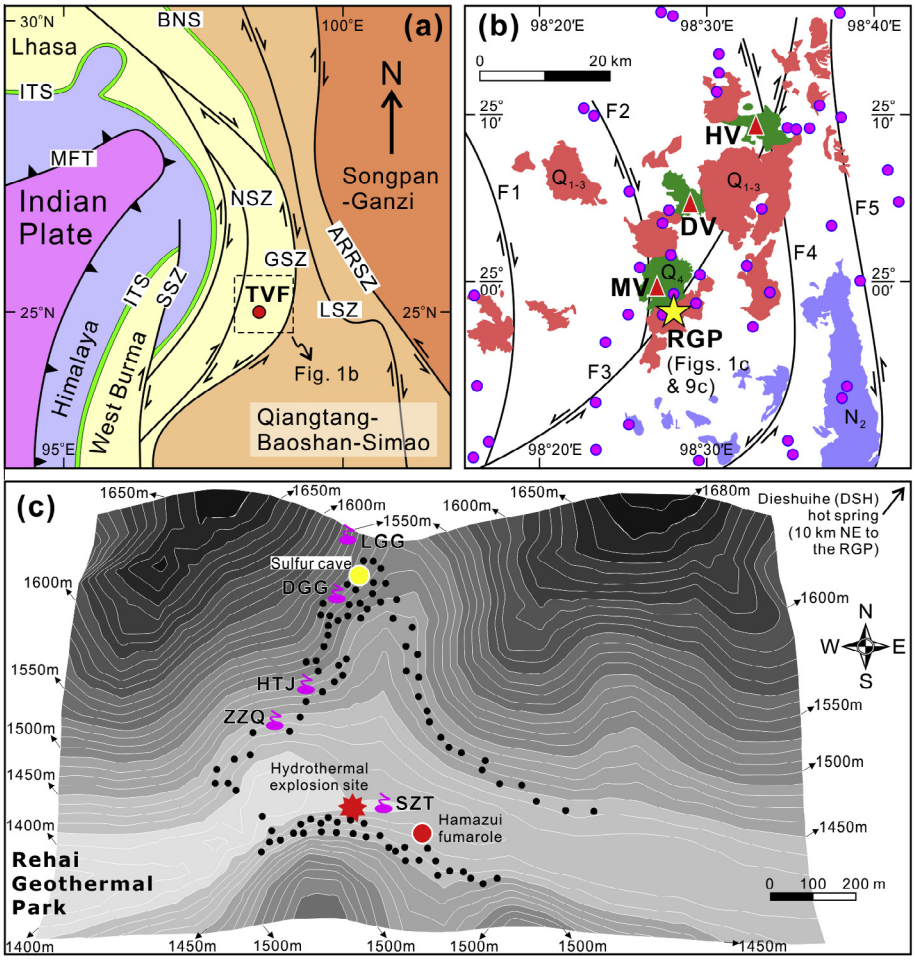

Fig. 1. (a) Regional map showing tectonic framework of southeastern Tibetan Plateau and Tengchong volcanic field (modified from Xu et al., 2015). Abbreviations: TVF, Tengchong volcanic field; ITS, Indus-Tsangpo suture; BNS, Bangong-Nujiang suture; MFT, Main frontal thrust; SSZ, Sagaing shear zone; NSZ, Nabang shear zone; GSZ, Gaoligong shear zone; LSZ, Lancangjiang shear zone; ARRSZ, Ailaoshan-Red River shear zone. (b) Sketch map showing distribution of the Rehai geothermal park (RGP), active volcanoes and Cenozoic volcanic rocks (N_2, Q_{1-3} and Q_4) in the TVF. Abbreviations: MV, Maanshan volcano; DV, Dayingshan volcano; HV, Heikongshan volcano. Major strike-slip faults are denoted as follows: F1, Binlangjiang fault; F2, Xinqi fault; F3, Dayingjiang fault; F4, Longchuan fault; F5, Longchuanjiang fault. Filled circles denote representative hot springs in the TVF. (c) Contour map showing major hot springs, fumarole and hydrothermal explosion in the RGP. Abbreviations: LGG, Laogunguo; DGG, Dagunguo; HTJ, Huaitaijing; ZZQ, Zhenzhuquan; SZT, Shizitou. Black dots represent locations of soil CO_2 flux survey.

hydrothermal volatiles. A genetic model involving subduction of the Indian continental lithosphere is proposed to explain chemical geodynamics of volatile recycling at continental subduction zone.

2. Geological setting

As an extended part of the southern Tibetan Plateau, Tengchong block is bounded by the Gaoligong shear zone to the east and the Indus-Tsangpo suture and Sagaing shear zone to the west (Fig. 1a). Cenozoic tectonic movement in response to the India-Asia continent collision and uplift of the Tibetan Plateau led to formation of a strike-slip fault system in the Tengchong block (e.g., Tapponnier et al., 2001; Wang et al., 2008; Xu et al., 2015), such as the Binlangjiang fault, Dayingjiang fault and Longchuanjiang fault (Fig. 1b; Huangfu and Jiang, 2000). Basement rocks of the Tengchong block are mainly composed of Precambrian metamorphic rocks, which are covered by Paleozoic-Mesozoic limestone, sandstone, mudstone and granitoids and Tertiary-Quaternary volcanic-sedimentary sequences (Huangfu and Jiang, 2000). High-K calc-alkaline volcanism in the TVF started in Late Miocene (ca. 8 Ma) and continued to historical period (i.e., CE 1609) with several interruptions, giving rise to widespread lava flows and pyroclastic rocks (e.g., Huangfu and Jiang, 2000; Zhou et al., 2012; Gao et al., 2015; Guo et al., 2015a). Holocene volcanic eruptions occurred at three active volcanoes (i.e., the Maanshan, Dayingshan and Heikongshan volcanoes; Fig. 1b), and in particular the Maanshan lavas are mainly composed of basaltic-andesitic volcanic rocks of mantle origin (Zhu et al., 1983; Wang et al., 2006; Zou et al., 2010).

Geophysical studies (e.g., Xu et al., 2012; Yang et al., 2013) have revealed the presence of low-velocity zone at crustal depth beneath active volcanoes in the TVF, possibly imaging crustal magma chamber that continuously provides material and heat for the overlying hydrothermal system. Modern hydrothermal activities in the TVF, such as hot spring (Fig. 2a), fumarole (Fig. 2b), hydrothermal explosion (Fig. 2c) and soil microseepage (Fig. 2d), are mainly distributed around active volcanoes and NE-SW-trending strike-slip faults (Fig. 1b). It is noted that >20 hydrothermal explosions have occurred in the RGP near Maanshan volcano since 1993 (Fig. 1c; Du et al., 2005), indicating high reservoir temperature related with continuous heating by crustal magma chamber. It mainly contains dry season (from November to April) and wet season (from May to October) in one year according to local meteorological records. For the TVF, the dramatic variation in precipitation between dry season and wet season would affect soil permeability and thus the intensity of soil CO_2 microseepage.

3. Analytical methods

Following accumulation chamber method reported in Chiodini et al. (1998), we carried out a soil CO_2 flux survey (including 91 points) using portable soil CO_2 flux meter (GXH-3010E) in the RGP during April 26th–28th, 2015. Before and during our fieldwork, Tengchong was rainy for several days as a signal of transition from dry season to wet season. Therefore, soil CO_2 flux survey in this study can reflect soil microseepage in wet season, while that of Cheng et al. (2014) can be regarded as case study in dry season. Detailed procedures for soil CO_2 flux measurement were described in M. Zhang et al. (2015). Outcropped surface with less influence from vegetation and human activities was chosen for soil CO_2 flux measurement. Edge of the inverted cylindrical chamber was sealed by tamped soil in order to diminish air contamination for accumulated soil gases (Lan et al., 2007; M. Zhang et al., 2015). Both soil temperatures (measured at depth of ca. 15 cm) and locations (measured by Garmin GPSMAP 60SCx) for each measurement point

Fig. 2. Photo showing hot spring (a, Dagunguo), fumarole (b, Hamazui), hydrothermal explosion site (c, photo provided by Libin Zhao from Tengchong Seismological Bureau) and soil microseepage (d, near sulfur cave) in the RGP.

were recorded to evaluate spatial distribution of soil CO_2 flux and temperature (see details in Supplementary Table S1).

Bubble gases were collected using pre-evacuated aluminum foil bags (M. Zhang et al., 2015) from hot springs in the RGP and adjacent region (Fig. 1c). Chemical and He-C isotopic compositions of collected samples were determined in Lanzhou Center for Oil and Gas Resources, Institute of Geology and Geophysics, Chinese Academy of Sciences, China. All samples were analyzed for chemical compositions using MAT 271 mass spectrometer. Helium isotopes were analyzed by Noblesse noble gas mass spectrometer, and carbon isotopes were analyzed by Delta Plus XP mass spectrometer. Detailed analytical procedures are described in Luo et al. (2014) and Li et al. (2014).

4. Results

4.1. Total CO_2 output of the TVF

Considering atmospheric pressure (85 kPa) as a function of local elevation (1450 m) and average air temperature (about 17 °C) during fieldwork, molar volume of gas was corrected for soil CO_2 flux calculation according to the Ideal Gas Law. Based on the modeling calculation method in Chiodini et al. (1998), a relatively broad range of soil CO_2 flux (6–2508 g m^{-2} d^{-1}; see details in Supplementary Table S1) was obtained, suggesting high variability and high intensity of soil microseepage in the RGP of the Tengchong active volcanic field (Fig. 3a). Spatial distribution of soil CO_2 fluxes is generally consistent with that of soil temperatures (Fig. 3). For example, high soil CO_2 fluxes (>800 g m^{-2} d^{-1}) are mainly located at the hydrothermal explosion site (Figs. 1c and 2c) and sulfur cave (Figs. 1c and 2d), where high soil temperatures (>30 °C) are also observed (Fig. 3b).

In order to evaluate CO_2 flux of soil microseepage in the RGP, a statistical method based on threshold estimation proposed by Sinclair (1974) was used to analyze background and anomalous data. As shown in cumulative probability plot (Fig. 4), soil CO_2 fluxes are basically divided into three groups (i.e., Groups A, B and C) by two inflections points at cumulative percentage of 51 and 93, respectively. Average soil CO_2 flux (42 g m^{-2} d^{-1}) of Group A represents background value of soil microseepage CO_2 flux in the RGP (Table 1). In contrast, anomalous data composed of both

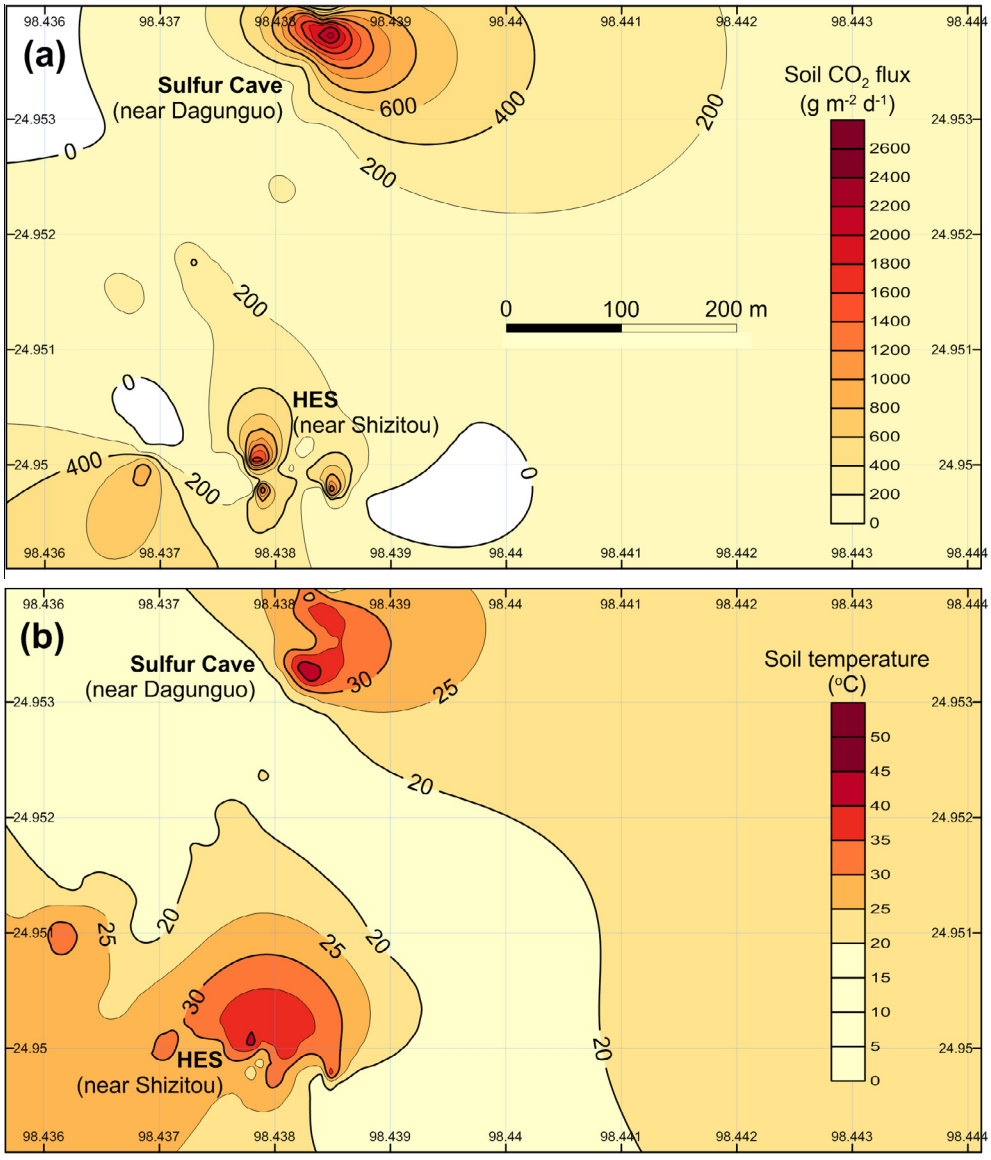

Fig. 3. Isogram showing distribution of soil CO_2 fluxes (a) and soil temperatures (b) in the RGP. Note that high soil CO_2 fluxes are consistent with high soil temperatures, as shown by HES (hydrothermal explosion site) and sulfur cave.

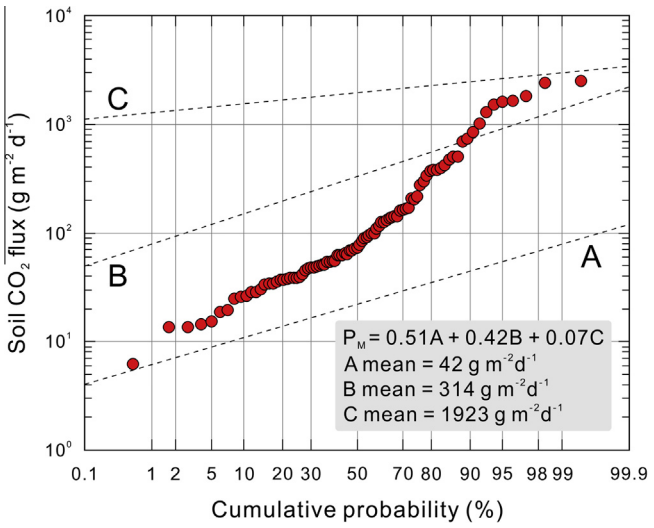

Fig. 4. Cumulative probability plot of calculated soil CO_2 fluxes in the RGP. Dashed lines represent the partition components of Groups A, B and C.

Table 1
Estimated parameters of Groups A, B and C of soil CO_2 fluxes in the RGP.

Group	Proportion (%)	Number of points	Average soil CO_2 flux with 95% confidence interval (g m^{-2} d^{-1})	Average total CO_2 output with 95% confidence interval (t d^{-1})
A	51	47	42 (39–46)	127 (116–138)
B	42	38	314 (257–371)	942 (772–1113)
C	7	6	1923 (1843–2004)	5770 (5528–6013)
Total	100	91	280 (177–383)	840 (532–1148)

Area = 3 km^2.

Group B and Group C are characterized by high average soil CO_2 flux (314 g m^{-2} d^{-1} and 1923 g m^{-2} d^{-1}, respectively; Table 1), indicating intensive soil microseepage in the RGP.

Average soil CO_2 flux in the RGP is about 280 g m^{-2} d^{-1} (Table 1), which is lower relative to that of soil CO_2 flux survey in November 2013 (ca. 875 g m^{-2} d^{-1}; Cheng et al., 2014), suggesting remarkable influence of continuous rainfall on soil permeability in wet season. Therefore, we conclude that average soil CO_2 flux in the RGP may vary from lower value (e.g., 280 g m^{-2} d^{-1}) in wet season to higher value (e.g., 875 g m^{-2} d^{-1}) in dry season. Based on outcrop of geothermal activities, total area of diffusive soil microseepage in the RGP and adjacent region is estimated at ca. 3 km^2 (Table 1), thus total soil CO_2 output would be about 840 t d^{-1} in wet season and 2625 t d^{-1} in dry season, yielding an average annual soil CO_2 output of about 6.30×10^5 t for the RGP and adjacent region. Combined with previously estimated CO_2 flux from hot springs (5.30×10^4 t a^{-1}; Cheng et al., 2012, 2014) and soil microseepage in other adjacent hydrothermal anomaly regions (3.80×10^6 t a^{-1}; Cheng et al., 2014), total CO_2 output of the whole TVF would be about 4.48×10^6 t a^{-1} (Table 2). Available data of CO_2 flux from soil microseepage and hot spring macroseepage in this study and previous studies (Cheng et al., 2012, 2014) indicate that, total CO_2 output of the TVF exhibits variation in a range of $(4.48–7.05) \times 10^6$ t a^{-1} (Table 2). It should be noted that total CO_2 output of the TVF will be updated along with further investigation of CO_2 flux in future. Additionally, our results would add new data to global volcanic subaerial CO_2 flux (5.40×10^8 t a^{-1}; Burton et al., 2013), contributing to the growing knowledge of deep carbon cycle at intra-continent subduction zone.

4.2. Chemical compositions

Bubble gas samples from hot springs in the RGP and adjacent region are generally characterized by high CO_2 (85.7–96.1%) and low H_2S (0–0.28%) contents (Table 3), similar to compositions of volatiles released by other active volcanoes in the world (e.g., Yang et al., 2005; Lowenstern et al., 2015; M. Zhang et al., 2015). It is noted that soil gas samples from the RGP also exhibit high CO_2 contents (Table 3; Cheng et al., 2014), consistent with high soil CO_2 flux of corresponding sampling site (e.g., sulfur cave; Figs. 1c and 2d). Considering comparable chemical and isotopic compositions, both bubble gas and soil gas samples are referred to the TVF samples for simplicity and clarity hereinafter.

N_2/Ar ratios of the TVF samples in this study range from 45 to 61, suggesting interaction between helium-rich components (mantle or crust; Taran, 2011) and air (N_2/Ar = 83.6, N_2/He = 1.49×10^5) or air-saturated water (ASW, N_2/Ar = 38, N_2/He = 2.64×10^5) as shown by linear trend from high-He/Ar to low-He/Ar endpoints (Fig. 5a). $CO_2/^3$He ratios (1.39×10^8–4.10×10^{11}; Fig. 5b) of the TVF samples overlap those of typical arc-related volatiles ($15.7 \pm 11 \times 10^9$; Sano and Williams, 1996) or upper mantle volatiles (2×10^9; Marty and Jambon, 1987), suggesting loss and/or addition of CO_2 during volatile migration in hydrothermal system (Van Soest et al., 1998; Hilton et al., 2002).

4.3. Helium isotopes

^{3}He/^{4}He ratios of the TVF samples range from 1.55 R_A to 5.27 R_A (where R_A = atmospheric ^{3}He/^{4}He = 1.39×10^{-6}; Mamyrin et al., 1970; Clarke et al., 1976), which are in good agreement with previously published data (e.g., Shangguan et al., 2000; Xu et al., 2004; Zhao et al., 2011, 2012). Compared with bubble gas samples (Fig. 6), soil microseepage gases are characterized by high ^{3}He/^{4}He (>3 R_A; Cheng et al., 2014), suggesting high mantle-derived ^{3}He flux in the RGP.

Air contamination of the studied samples can be observed from positively correlated ^{3}He/^{4}He and ^{4}He/^{20}Ne between mantle end-

Table 2
CO_2 fluxes of the TVF and representative active volcanic fields in the world.

Active volcanoes	Country	Soil CO_2 flux (t a^{-1})	Dissolved CO_2 flux (t a^{-1})	Total CO_2 flux (t a^{-1})	Data source
Tengchong	China	4.43×10^6	5.30×10^4	4.48×10^6	This study
Tengchong	China	7.00×10^6	5.30×10^4	7.05×10^6	Cheng et al. (2012, 2014)
Changbaishan	China	7.79×10^5	6.90×10^4	8.48×10^5	Zhang et al. (2011) and Guo et al. (2014b)
Yangbajing	China	8.60×10^4	Not detected	8.60×10^4	Zhang et al. (2014)
Vulcano	Italy	4.20×10^4	2.19×10^3	4.42×10^4	Inguaggiato et al. (2012)
Stromboli	Italy	8.21×10^4	Not detected	8.21×10^4	Carapezza and Federico (2000)
Etna	Italy	1.00×10^6	2.50×10^5	1.25×10^6	D'Alessandro et al. (1997)
Yellowstone	USA	1.64×10^7	Not detected	1.64×10^7	Werner and Brantley (2003)
Ukinrek Maars	USA	1.18×10^4	1.10×10^3	1.29×10^4	Evans et al. (2009)
Hakkoda	Japan	2.70×10^4	Not detected	2.70×10^4	Hernández et al. (2003)
Iwojima	Japan	1.64×10^5	Not detected	1.64×10^5	Notsu et al. (2005)

Table 3
Chemical and He-C isotopic compositions of the TVF hydrothermal volatiles.

Sample no.	Sample locality	Sample type	T[a] (°C)	N_2 (%)	O_2 (%)	Ar (%)	H_2S (%)	CO_2 (%)	CH_4 (%)	He (ppm)	$^4He/^{20}Ne$	R_m/R_A	R_C/R_A	Helium inventory (%)			$\delta^{13}C\text{-}CO_2$ (‰)	$CO_2/^3He$ ($\times10^9$)	Data source
														Mantle	Crust	Air			
LGG01	LGG	BG	62.8	2.51	0.87	0.05	0.11	95.9	0.38	49.8	29.7	3.22	3.25	40.0	59.0	1.00	−3.02	4.30	This study
LGG02	LGG	BG	62.5	2.40	0.86	0.05	0.09	96.1	0.39	56.0	86.4	3.53	3.53	43.9	55.8	0.30	−3.71	3.50	This study
HTJ01	HTJ	BG	91.5	5.62	1.59	0.11	0.05	92.0	0.05	5.15[b]	–	–	–	–	–	–	–	–	This study
HTJ02	HTJ	BG	90.8	3.84	1.09	0.09	0.04	94.3	0.05	5.15	2.03	2.86	3.15	33.6	50.7	15.6	−3.81	46.1	This study
ZZQ01	ZZQ	BG	93.4	7.98	2.77	0.13	0.28	88.7	0.03	3.82	1.45	2.74	3.21	31.4	46.7	21.9	−4.92	60.9	This study
ZZQ02	ZZQ	BG	94.1	4.52	1.94	0.10	0.25	93.0	0.05	3.82[c]	–	–	–	–	–	–	–	–	This study
SZT01	SZT	BG	59.7	8.66	3.39	0.16	0.0	87.8	0.03	2.09	0.62	1.58	2.11	13.2	35.5	51.3	−2.07	192	This study
SZT02	SZT	BG	58.5	8.03	3.03	0.14	0.0	88.8	0.03	2.12	0.84	1.55	1.85	14.5	47.7	37.8	−3.03	195	This study
DSH01	DSH	BG	19.8	11.9	2.08	0.23	0.0	85.7	0.0	338	148	4.37	4.37	54.4	45.4	0.20	−5.96	0.42	This study
DSH02	DSH	BG	20.5	11.4	2.07	0.23	0.0	86.2	0.0	331	162	4.33	4.34	54.0	45.8	0.20	−5.59	0.43	This study
110117-DSH[d]	DSH	BG	23.6	11.7	2.08	0.23	0.0	86.0	0.0	99.4	28.7	5.27	5.30	65.6	33.3	1.10	−9.00	1.18	This study
110118-HH	HH	BG	71.5	–	–	–	–	–	–	4.91	2.09	2.75	2.99	32.3	52.5	15.2	−5.50	–	This study
SZT05	HES	SG	24.3	6.30	0.50	0.06	0.0	93.1	0.01	15.0	8.70	3.36	3.43	41.4	55.0	3.60	−4.74	13.3	Cheng et al. (2014)
SZT12	HES	SG	26.5	2.80	0.50	0.03	0.0	96.6	0.19	21.0	4.50	4.04	4.22	49.5	43.5	7.00	−4.80	8.19	Cheng et al. (2014)
LTQ02	SC	SG	31.7	3.20	0.50	0.04	0.11	95.6	0.61	64.0	28.1	3.48	3.50	43.2	55.7	1.10	−3.68	3.09	Cheng et al. (2014)

Abbreviations for sample localities (Fig. 1c) are as follows: LGG, Laogunguo; HTJ, Huaitaijing; ZZQ, Zhenzhuquan; SZT, Shizitou; DSH, Dieshuihe; HH, Hehua; HES, hydrothermal explosion site; SC, sulfur cave. Sample type: BG, bubble gas; SG, soil gas. Measured $^3He/^4He$ ratios (R_m/R_A) have been calibrated for air contamination using air-normalized He/Ne ratio multiplied by the ratio of their Bunsen coefficients (Weiss, 1971), assuming a groundwater recharge temperature of 10 °C (see details in Hilton, 1996). Corrected $^3He/^4He$ ratio is reported in R_C/R_A notation, where R_C denotes air-corrected $^3He/^4He$ ratio and R_A represents $^3He/^4He$ ratio of air, i.e., 1.39×10^{-6} (Mamyrin et al., 1970; Clarke et al., 1976).

[a] T represents temperature.

[b] Helium content of sample HTJ01 is assumed to be identical with that of sample HTJ02.

[c] Helium content of sample ZZQ02 is assumed to be identical with that of sample ZZQ01.

[d] Chemical compositions (except for helium) of sample 110117-DSH are assumed to be average of samples DSH01 and DSH02.

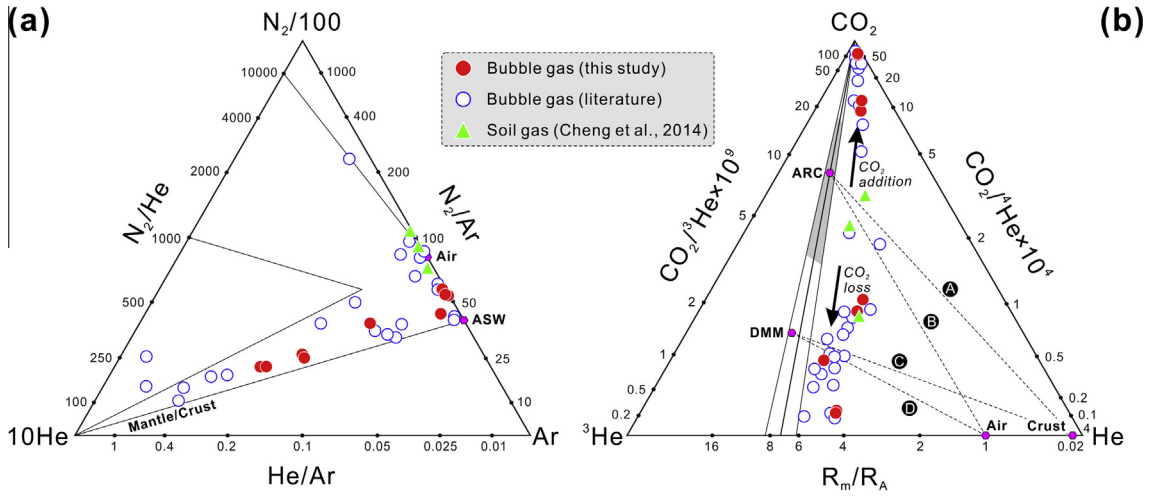

Fig. 5. Triangle plots of N_2-He-Ar (a) and versus CO_2-^{3}He-^{4}He (b) for the TVF samples (modified from Giggenbach and Poreda, 1993; Taran, 2011). Data are shown with previously published data from Shangguan et al. (2000), Xu et al. (2004), Zhao et al. (2011, 2012) and Cheng et al. (2014). Abbreviations are as follows: ASW, air-saturated water; ARC, arc-related volatiles; DMM, depleted MORB-source mantle. Dashed lines represent contamination of arc-related volatiles (Lines A and B) and DMM-derived volatiles (C and D) by crust and air, respectively. Gray area denotes reference range of ^{3}He/^{4}He (7.4 ± 1.3 R_A; Sano and Fischer, 2013) and CO_2/^{3}He (15.7 ± 11 × 10^9; Sano and Williams, 1996) for arc-related volatiles.

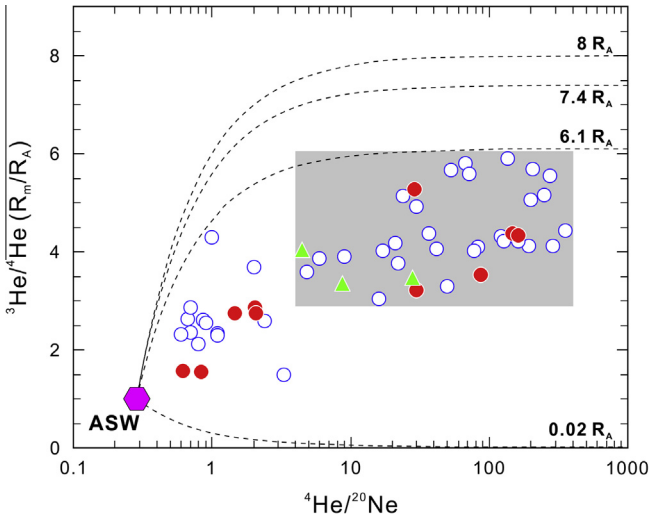

Fig. 6. ^{3}He/^{4}He (R_m/R_A) vs. ^{4}He/^{20}Ne for the TVF samples. Calculated binary mixing curves between air-saturated water (ASW), upper mantle (DMM) and sub-continental lithospheric mantle (SCLM), arc-related component (ARC) and crust are shown. Reference values for end-members are as follows: ASW, ^{3}He/^{4}He = 1 R_A, ^{4}He/^{20}Ne = 0.285 (Ozima and Podosek, 1983); DMM, ^{3}He/^{4}He = 8 ± 1.5 R_A (Sano and Fischer, 2013); ARC, ^{3}He/^{4}He = 7.4 ± 1.3 R_A (Sano and Fischer, 2013); SCLM, ^{3}He/^{4}He = 6.1 ± 0.9 R_A (Gautheron and Moreira, 2002); Crust, ^{3}He/^{4}He = 0.02 R_A (Lupton, 1983). In the latter 4 cases a ^{4}He/^{20}Ne ratio 1000 is assumed. Symbols are as in Fig. 5.

member and air/ASW (Fig. 6). Therefore, air-derived helium contribution should be corrected before constraining origin and evolution of the TVF hydrothermal volatiles (Ozima and Podosek, 1983; Rison and Craig, 1983; Hilton, 1996). A correction method involving both air- and water-derived helium as contaminant was adopted to correct measured ^{3}He/^{4}He ratios to their "true" values [see details in Hilton (1996)]. In addition, if samples do not have measured N_2/Ar ratios that range from ASW value (N_2/Ar = 38 at 0 °C) to air value (N_2/Ar = 83.6), the ASW correction method that assuming all sample ^{20}Ne originates from air dissolved in water was applied for atmospheric helium correction (Craig et al., 1978). Air-corrected ^{3}He/^{4}He ratios (1.85–5.30 R_A; Table 3) of the TVF samples are lower than those of depleted mid-ocean ridge basalt (MORB)-source mantle (DMM, 8.0 ± 1.5 R_A; Sano and Fischer, 2013) and sub-continental lithospheric mantle (SCLM, 6.1 ± 0.9 R_A; Gautheron and Moreira, 2002). Additionally, contributions from an end-member with high radiogenic ^{4}He can be confirmed by lower ^{3}He/^{4}He ratios of the TVF samples relative to arc-related volatiles (7.4 ± 1.3 R_A; Sano and Fischer, 2013).

4.4. Carbon isotopes

δ^{13}C-CO_2 values of the TVF samples range from −9.00‰ to −2.07‰ (Table 3), in agreement with those reported for typical arc-related volcanic volatiles (−9.8‰ to −1.3‰; Marty et al., 1989; Varekamp et al., 1992; Sano and Marty, 1995; Sano and Williams, 1996). Compared with upper mantle values (−6.5 ± 2.5‰; Pineau and Javoy, 1983), some TVF samples have relatively heavier carbon isotopic compositions, suggesting possible contribution from carbonate (0 ± 2‰; Hoefs, 2009).

5. Discussion

Magma-derived volatiles tend to be affected by both deep and shallow processes en route to the atmosphere (Giggenbach, 1996; Sano and Fischer, 2013), such as volatile exsolution from magmas and hydrothermal fluids (Giggenbach and Poreda, 1993; Dixon, 1997; Hilton et al., 1998), calcite precipitation in response to fluid cooling (Hahm et al., 2008), and contamination by crustal materials in hydrothermal system (Hilton et al., 1993; Shaw et al., 2003; Sano and Fischer, 2013). Based on helium inventory calculation for samples in literature and this study (Table 3), only samples with high ^{4}He/^{20}Ne (>4) are focused in the following discussion in order to diminish influence from air contamination.

5.1. Controls on He-CO_2 systematics

Variations in CO_2/^{3}He ratios are generally expected for volatiles released by volcanic-hydrothermal system, owing to multi-components mixing (Barry et al., 2013) and/or elemental fractionation induced by different solubilities of CO_2 and helium in melts/fluids (Hilton et al., 1998; Ray et al., 2009; Iacono-Marziano et al., 2010). It is noted that the TVF samples with ^{4}He/^{20}Ne > 4 exhibit larger range of CO_2/^{3}He (1.37 × 10^8–1.23 × 10^{11}) relative to that

of either arc-related volatiles or DMM-derived volatiles (Figs. 5b and 7). Moreover, most of the TVF volatiles (especially the high-R_A samples) have lower $CO_2/^3He$ compared to enriched mantle wedge (EMW; Fig. 7a), which is considered as source region of the TVF magmas and volatiles (see details in Section 5.2). Therefore, we suggest that remarkable loss of CO_2 is required to explain low $CO_2/^3He$ ratios of volatiles released by the EMW-derived melts beneath Maanshan volcano. Possible mechanisms responsible for CO_2 loss mainly include magma degassing in a closed-system magma chamber (Javoy et al., 1978; Hilton et al., 1998; Roulleau et al., 2015a) and calcite precipitation in hydrothermal system (Hahm et al., 2008; Ray et al., 2009).

A prominent signature observed in He-CO_2 systematics of the TVF volatiles is the negatively correlated $CO_2/^3He$ and $^3He/^4He$ (Fig. 7a), which can be attributed to crustal contamination. Namely, high $CO_2/^3He$ of low-R_A samples might result from contamination by crustal materials with low $^3He/^4He$ (0.02 R_A; Lupton, 1983) and high $CO_2/^3He$ (10^{12}–10^{14}; O'Nions and Oxburgh, 1988). Considering relatively high $\delta^{13}C\text{-}CO_2$ and $CO_2/^3He$ for low-R_A samples (Figs. 7b and 8), the most likely contaminant

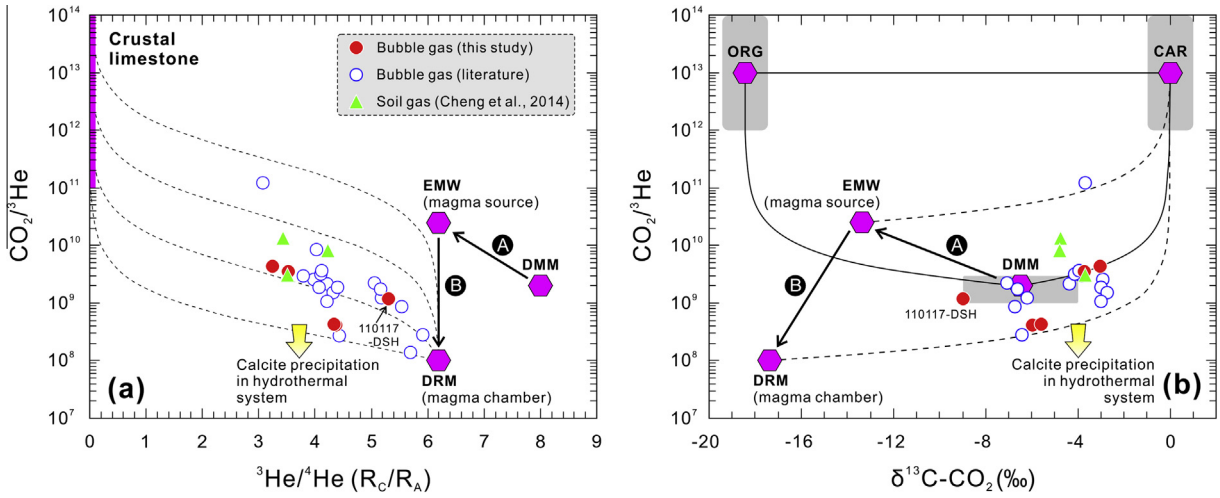

Fig. 7. $CO_2/^3He$ vs. $^3He/^4He$ (a) and $CO_2/^3He$ vs. $\delta^{13}C\text{-}CO_2$ (b) for the TVF samples. Abbreviations: DMM, depleted MORB-source mantle; EMW, enriched mantle wedge; DRM, degassed residual melts; CAR, subducted and crustal limestones; ORG, subducted organic metasediments. Dashed curves represent contamination of degassed volatiles by crustal limestone. Reference values for end-members are as follows: DMM, $^3He/^4He$ = 8 ± 1.5 R_A (Sano and Fischer, 2013), $\delta^{13}C\text{-}CO_2$ = −6.5 ± 2.5‰ (Pineau and Javoy, 1983), $CO_2/^3He = 2 \times 10^9$ (Marty and Jambon, 1987); ORG, $^3He/^4He$ = 0.02 R_A (Lupton, 1983), $\delta^{13}C\text{-}CO_2$ = −18.45‰ (Cook-Kollars et al., 2014), $CO_2/^3He = 10^{13}$ (O'Nions and Oxburgh, 1988); CAR, $^3He/^4He$ = 0.02 R_A (Lupton, 1983), $\delta^{13}C\text{-}CO_2$ = 0‰ (Hoefs, 2009), $CO_2/^3He = 10^{11}$–10^{14} (O'Nions and Oxburgh, 1988). He-C elemental and isotopic compositions of the EMW ($^3He/^4He$ = 6.19 R_A, $\delta^{13}C\text{-}CO_2$ = −13.4‰, $CO_2/^3He = 2.49 \times 10^{10}$) are calculated according to best-fit ternary mixing in mantle wedge (see details in Fig. 8). $CO_2/^3He$ of the DRM is assumed to be 10^8, which theoretically represents the lowest $CO_2/^3He$ of the EMW-derived residual melts if calcite precipitation effect on drawdown of $CO_2/^3He$ is not considered. Arrow A represents mantle wedge enrichment induced by recycling of crustal materials from subducted Indian continental lithosphere. Arrow B represents continuous degassing of the EMW-derived residual melts in a closed-system magma chamber, which can explain low $CO_2/^3He$ ratios of relatively less contaminated samples. Volatiles released by residual melts in magma chamber tend to be affected by calcite precipitation in hydrothermal system.

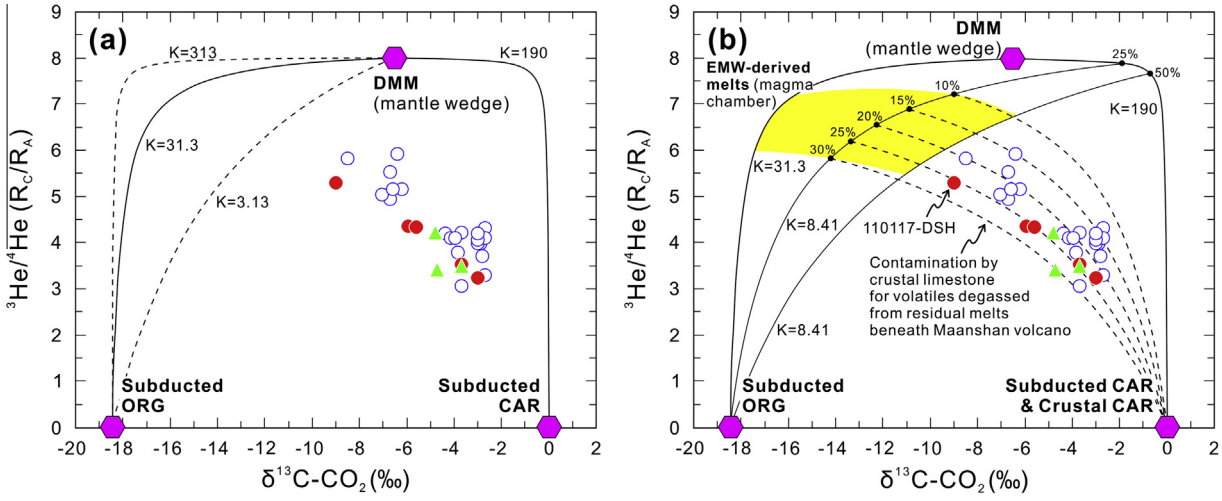

Fig. 8. He-C isotope coupling model showing mantle wedge enrichment and crustal contamination by limestone for the TVF samples. Abbreviations are as in Fig. 7. Reference values for end-members are listed in Supplementary Table S2. K value [= $(He/C)_A/(He/C)_B$] represents curvature of mixing curve between end-member A and end-member B. (a) Dashed curves represent upper and lower limits for mixing between DMM and subducted ORG end-member, while solid curves represent best-fit scenario for DMM-ORG mixing (K = 31.3) and DMM-CAR mixing (K = 190). (b) Numbers (25% and 50%) on K = 190 curve represent proportion of subducted limestone in DMM-CAR mixing, which is constrained by He-C isotopic compositions of the high-R_A samples. Numbers (10%, 15%, 20%, 25% and 30%) on K = 31.3 curve represent proportion of subducted organic metasediments in mixing between DMM-CAR mixture and subducted ORG components. Yellow area represents possible He-C isotope range of the EMW. Given that sample 110117-DSH might have undergone less crustal contamination relative to other samples, selected He-C elemental and isotopic compositions of the EMW (Fig. 7) are calculated if proportion of subducted ORG end-member is assumed to be 25% (i.e., DMM-CAR-ORG proportion = 56:19:25). Dashed curves represent crustal contamination by crustal limestone for volatiles released by residual melts.

for the TVF samples is crustal limestone. Although magma degassing and calcite precipitation contributed to drawdown of $CO_2/^3He$ ratios, they cannot explain negative correlation between $CO_2/^3He$ and $^3He/^4He$ of the TVF samples (Fig. 7a). In other words, if contamination by crustal limestone is not taken into account, it would be unrealistic to expect higher degrees of magma degassing and/or calcite precipitation for high-R_A samples, and vice versa. We suggest that coupled low $CO_2/^3He$ and high $^3He/^4He$ can be interpreted as nature of initially degassed volatiles from residual melts that have been affected by continuous magma degassing. And more importantly, crustal contamination would act as the first-order control on systematic variations in $CO_2/^3He$ and He-C isotopes of the TVF volatiles. These physical and chemical processes can be quantitatively constrained by mixing curves between initially degassed volatiles and crustal limestone (Fig. 7).

In details, recycling of crustal materials from the Indian continent into asthenosphere would lead to formation of enriched mantle wedge (represented by Arrow A; Fig. 7), which is interpreted as source region of the TVF parental magmas (Guo et al., 2015a). Continuous magma degassing in a closed-system magma chamber (represented by Arrow B; Fig. 7) may be expected for residual melts beneath Maanshan volcano since its latest eruption (7.5 ± 1.0 ka; Wang et al., 2000), because: (1) magmatic zircons from Holocene Maanshan lavas reveal a closed-system magma chamber with neglectable influence from magma-country rock interaction (Zou et al., 2010, 2014), and (2) the EMW-derived magma recharge may have not occurred since the last eruption of Maanshan volcano (if not, $CO_2/^3He$ ratios of high-R_A samples would be significantly higher than observed values). Considering time of the latest eruption of Maanshan volcano and time-dependent variations of magma $^3He/^4He$ (Torgersen and Jenkins, 1982; Sano and Nakajima, 2008; Moreira, 2013; Sano and Fischer, 2013), magma degassing and aging effect can be neglectable for helium isotopic composition of residual melts. In the case of batch equilibrium degassing (closed-system), CO_2 loss would lower $\delta^{13}C$-CO_2 value of residual CO_2 by an isotope fractionation factor of −4‰ (Javoy et al., 1978), as denoted by degassed residual melts (DRM; Fig. 7b). Calcite precipitation at variable temperatures may have pervasively occurred to volatiles in hydrothermal system, but it did not change correlations between $CO_2/^3He$ ratios and He-C isotopes of the TVF samples (Fig. 7).

5.2. Chemical geodynamics of volatile recycling at continental subduction zone

5.2.1. Mantle wedge enrichment related with continental subduction

Geochemical studies on Maanshan lavas reveal an enriched mantle source (Wang et al., 2006; Zou et al., 2014), which might be generated by addition of slab fluids into mantle wedge owing to eastward underthrusting of the Indian continental lithosphere (Guo et al., 2015a). Similar to volatile recycling at oceanic subduction zone (Sano and Marty, 1995), considerable radiogenic ^4He and other volatiles can be transported into mantle wedge (DMM; Guo et al., 2015a) by subducted organic metasediment (ORG) and carbonate (CAR) from Indian continent, leading to formation of an enriched mantle wedge. The recycled volatiles (e.g., carbon, nitrogen and helium) would then return back into atmosphere through subduction zone volcanism (Staudacher and Allègre, 1988; Sano et al., 2001; Poli et al., 2009; Kelemen and Manning, 2015; Kagoshima et al., 2015). Although the SCLM can also provide high mantle ^3He contribution (Gautheron and Moreira, 2002), it will not be focused in this study because mantle enrichment processes induced by recycling of crustal materials are theoretically similar for the DMM and SCLM. And particularly, the former scenario is consistent with asthenospheric origin of the TVF magmas (Guo et al., 2015a), and is more easily to be quantitatively constrained.

For the TVF hydrothermal volatiles, the ORG end-member can be proxied by organic matter ($\delta^{13}C = -25‰$ to $-22‰$; Ramaswamy et al., 2008) from the Indo-Burman Ranges in eastern Indian continental margin [e.g., the Irrawaddy sediments; Guo et al. (2015a) and references therein]. Given that subduction zone metamorphism can transfer $\delta^{13}C$ values of typical organic sediments to heavier values (Bebout, 1995), an average $\delta^{13}C$ value (−18.45‰; Cook-Kollars et al., 2014) of metamorphosed organic matter is taken as that of subducted ORG end-member. On the other hand, subducted CAR end-member can be represented by limestones from the Indo-Burman Ranges (e.g., the Albian limestones in the Upper Irrawaddy basin; Mitchell, 1993), and their $\delta^{13}C$ values theoretically vary in 0 ± 2‰ (Shields and Veizer, 2002; Hoefs, 2009). Following method in Van Soest et al. (1998), both ORG and CAR end-members have $^3He/^4He$ ratio that equals that of bulk continental crust (0.02 R_A; Lupton, 1983). Other reference values for associated parameters of the DMM, CAR and ORG end-members are listed in Supplementary Table S2.

As shown in the He-C isotope coupling model (Fig. 8a), the TVF samples are all enclosed by DMM-CAR mixing curve and DMM-ORG mixing curve, indicating that a ternary mixing model involving DMM, CAR and ORG end-members is required to explain their He-C isotope systematics. An enriched mantle wedge (represented by the yellow area in Fig. 8b) can be generated by mixing of recycled materials and mantle due to subduction of the Indian continental lithosphere, which is consistent with geophysical (e.g., Huang and Zhao, 2006; Lei and Zhao, 2016) and geochemical (e.g., Guo et al., 2015a) studies (Figs. 9a and 9b). According to He-C isotopes of the high-R_A samples (Fig. 8b), the maximum proportion of subducted limestone in DMM-CAR mixing (K = 190 curve) may be about 50%, while proportion of subducted organic metasediment may range from 10% to 30% in mixing of DMM-CAR mixture and subducted ORG end-member (K = 8.41 curve with 25%-CAR endpoint). Otherwise, calculated He-C isotopic compositions of the EMW would overlap the TVF hydrothermal volatiles (e.g., sample 110117-DSH), in contrast to the predominant control of crustal contamination on their He-C isotope systematics. In other words, it is straightforward that negative correlation between $^3He/^4He$ and $\delta^{13}C$ reflects contamination by crustal limestone, rather than sampling different parts of the EMW with variable degrees of mantle wedge enrichment.

5.2.2. Crustal contamination of the EMW-derived volatiles

The RGP and adjacent region is cut by several N-S- and NW-SE-trending faults (Shangguan et al., 2004), which can act as pathways for penetration of meteoric water into underground hydrothermal system. On the contrary, the strike-slip fault system would also be passage for mantle helium and carbon released by the EMW-derived melts (Fig. 9c). It is noted that crustal limestones pervasively outcrop in upper crust of the TVF (Zhang et al., 1996), which are likely to be country rock of the hydrothermal system (Fig. 9c). Owing to interaction between recharging meteoric water and limestone, hydrothermal fluids would be enriched in radiogenic ^4He and CO_2 and act as contaminants for degassed volatiles from the EMW-derived residual melts, which can explain the expected crustal contamination of the TVF samples from hot springs and soil microseepage.

Given that average proportion of subducted limestone might be 25% for binary mixing between DMM and subducted CAR end-member, we take 75:25 as the representative proportion between depleted mantle wedge and subducted limestone (Fig. 8b). Therefore, K = 8.41 curve with 25%-endpoint would represent the best-fit ternary mixing scenario for formation of the EMW. It is noted that the TVF samples are all plotted on the best-fit mixing curves between the EMW-derived melts and crustal limestone (Fig. 8b), which clearly supports the first-order control of crustal contamina-

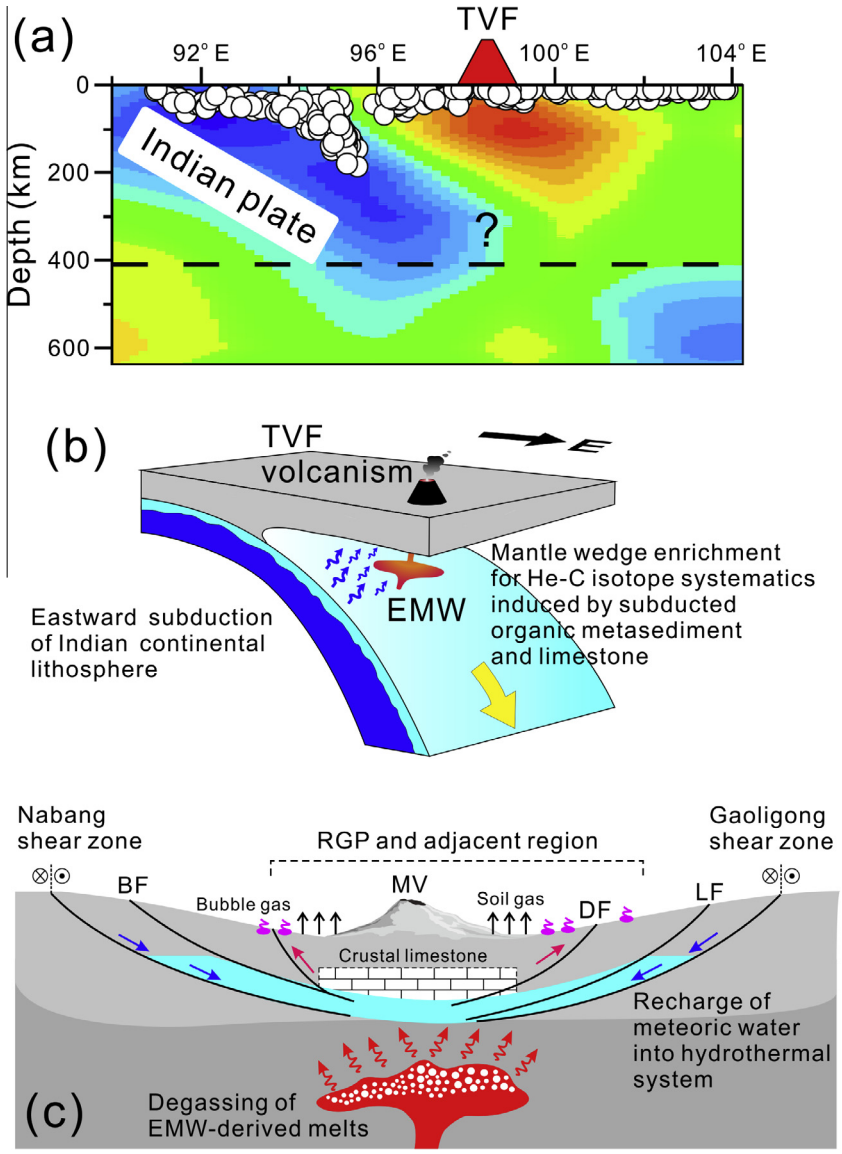

Fig. 9. (a) High-resolution P wave tomographic model showing subduction of Indian continental lithosphere beneath the TVF (modified from Huang and Zhao, 2006). The open circles represent earthquakes that occurred in subducted Indian plate and the Asian lithosphere (Huang and Zhao, 2006). (b) Schematic map showing formation of enriched mantle wedge as a result of eastward subduction of Indian continental lithosphere (modified from Guo et al., 2015a). (c) Contamination of volatiles degassed from residual melts by crustal limestone. Abbreviations: RGP, Rehai geothermal park; MV, Maanshan volcano; BF, Binlangjiang fault; DF, Dayingjiang fault; LF, Longchuanjiang fault.

tion on their He-CO_2 systematics. Given that sample 110117-DSH might have undergone less crustal contamination relative to other samples, calculated He-C elemental and isotopic compositions of the 25%-endpoint on dashed curve across sample 110117-DSH can represent those of the EMW. As shown in Fig. 7, the validity of calculated He-C isotopes of the EMW can also be verified by mixing curves between EMW-derived melts (and DRM) and crustal limestone.

5.2.3. Implications for deep carbon cycle at continental subduction zone

For carbon inventory of the TVF hydrothermal volatiles, source components are derived from asthenospheric mantle (DMM), subducted organic sediments (ORG), subducted and crustal limestones (CAR), which is consistent with carbon recycling model at subduction zone (Sverjensky et al., 2014). Relative proportions of the DMM, ORG and CAR end-members can be calculated following equations proposed by Sano and Marty (1995), which are as follows:

$$(^{13}C/^{12}C)_{Obs} = (^{13}C/^{12}C)_{DMM} \cdot M + (^{13}C/^{12}C)_{ORG} \cdot S + (^{13}C/^{12}C)_{CAR} \cdot L$$

$$1/(^{12}C/^{3}He)_{Obs} = M/(^{12}C/^{3}He)_{DMM} + S/(^{12}C/^{3}He)_{ORG} + L/(^{12}C/^{3}He)_{CAR}$$

$$M + S + L = 1$$

where subscripts Obs, DMM, ORG and CAR refer to observed sample, depleted MORB-source mantle, organic sediments and carbonate (including subducted and crustal limestones), respectively. Proportions of DMM, CAR and ORG end-members are presented by M, S and L, respectively. Reference values for end-member parameters are as previous studies (Sano and Marty, 1995; Sano and Williams, 1996; M. Zhang et al., 2015), which are DMM: $\delta^{13}C = -6.5‰$, $CO_2/^3He = 2 \times 10^9$; ORG: $\delta^{13}C = -18.45‰$, $CO_2/^3He = 10^{13}$; CAR: $\delta^{13}C = 0‰$, $CO_2/^3He = 10^{13}$. In our calculation, subducted limestone (as agent for mantle wedge enrichment) and crustal limestone (as contaminant for the TVF samples) are assumed to have identical $\delta^{13}C$ value (0‰; Hoefs, 2009) and $CO_2/^3He$ ratio (10^{13}; O'Nions and Oxburgh, 1988).

Considering pervasive He-C elemental fractionation due to magma degassing and calcite precipitation, only a few TVF samples enclosed by mixing curves between DMM, ORG and CAR end-members can yield reasonable calculation results (Fig. 7b). Average proportions of upper mantle, subducted sediments and limestones are about 47%, 8% and 45% (Table 4), respectively. However, it should be noted that relative proportion of subducted and crustal limestones cannot be distinguished from each other solely by ternary mixing calculation of Sano and Marty (1995). Furthermore, end-member proportions calculated by above ternary mixing method are likely to be affected by calcite precipitation. With this respect, we suggest that He-C elemental fractionation would exert limited influence on He-C isotope coupling model, which can roughly yield proportions of crustal limestone and mantle-derived components. In details, the crustal CAR end-member would contribute about 15–55% to the total carbon inventory, while the rest carbon (about 45–85%) originates from the EMW. Therefore, mantle-derived magmas at intra-continent subduction zone, which provide abundant CO_2-rich volatiles and continuous heat for overlying hydrothermal system (Fig. 9), can act as important triggers for liberation of carbon stored in crustal carbonate rocks (e.g., limestone). Based on origin and evolution of the TVF volatiles, we suggest that volatile recycling at the India-Asia continental subduction zone has the potential to be a complement to volatile recycling mechanism at subduction zones (Lee et al., 2013; Lee and Lackey, 2015).

5.2.4. Identification of volatile recycling model at continental subduction zone

Volatiles released from different types of plate boundaries, such as mid-ocean ridge (MOR), oceanic subduction zone (OSZ), continental subduction zone (CSZ) and continental collision zone (CCZ), are expected to display discernible geochemical signatures. Eastward underthrusting of the Indian continental lithosphere into asthenosphere beneath the TVF has been revealed by recent geophysical and geochemical studies (Huang and Zhao, 2006; Lei et al., 2013; Guo et al., 2015a). Combined with the He-C isotope coupling model, we suggest that the TVF samples can represent volatiles released from CSZ, making it reasonable to compare geochemical signatures between volatiles from MOR, OSZ, CSZ and CCZ.

As shown in histogram of helium isotopes (Figs. 10a and 10b), air-corrected $^3He/^4He$ ratios of the TVF samples (0.21–5.92 R_A) are clearly lower relative to reference values for arc-related volatiles (7.4 ± 1.3 R_A; Sano and Fischer, 2013) and many typical OSZ samples [0.03–8.46 R_A; e.g., Kamchatka (Taran, 2009), Japan Arc (Sano et al., 1994, 1998, 2006; Roulleau et al., 2015b), Sunda Arc (Halldórsson et al., 2013) and Lesser Antilles (Jean-Baptiste et al., 2014)]. Compared with MOR values (e.g., 8.0 ± 1.5 R_A; Sano and Fischer, 2013), $^3He/^4He$ ratios of volatiles from convergent plate boundaries tend to be lower (Figs. 10a, 10b and 10c), owing to (1) addition of recycled crustal materials into mantle source region (e.g., M. Zhang et al., 2015), (2) magma degassing and aging effect in magma chamber (e.g., Moreira, 2013; Sano and Fischer, 2013)

Table 4
Carbon inventory estimated by ternary mixing calculation for the TVF hydrothermal volatiles.

Sample no.	$\delta^{13}C$-CO_2 (‰)	$CO_2/^3He$ ($\times10^9$)	Carbon inventory (%)			Data source
			DMM	ORG	CAR	
LGG01	−3.02	4.31	46	0.0	54	This study
LGG02	−3.71	3.94	51	2.0	47	This study
SZT05	−4.74	13.4	15	20	65	Cheng et al. (2014)
SZT12	−4.80	8.31	24	18	58	Cheng et al. (2014)
RH-Dadijiao	−3.94	3.61	55	2.0	43	Xu et al. (2004)
Dieshuihe	−7.07	2.22	90	7.0	3.0	Xu et al. (2004)
Average	−4.55	5.97	47	8.0	45	

Abbreviations: DMM, depleted MORB-source mantle; ORG, organic metasediments; CAR, limestone.

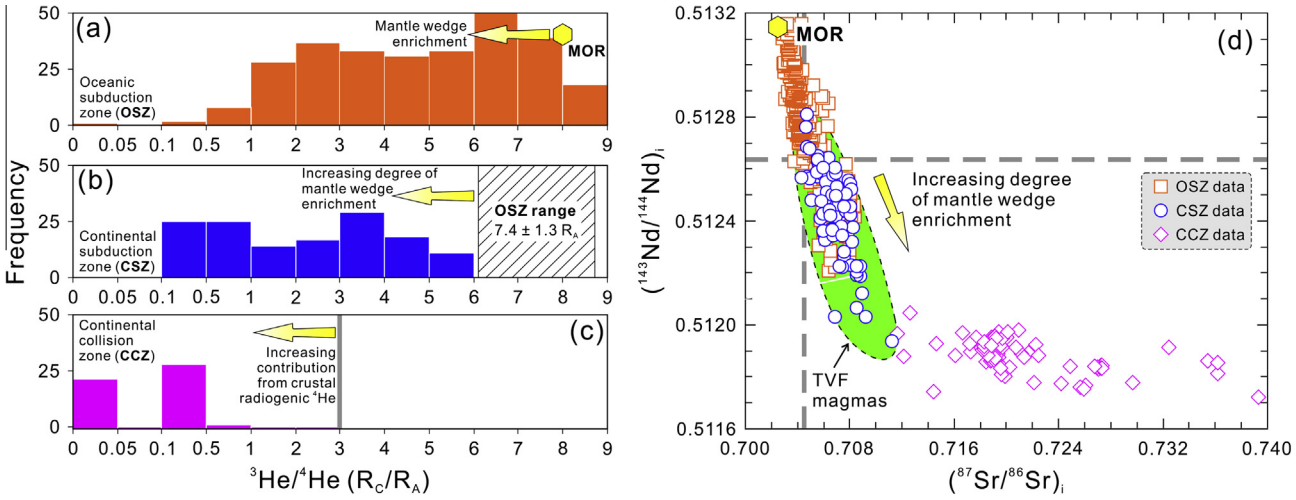

Fig. 10. (a) Comparison of helium isotopes between volatiles from MOR (Graham, 2002; Sano and Fischer, 2013), OSZ (Sano et al., 1994, 1998, 2006; Taran, 2009; Halldórsson et al., 2013; Jean-Baptiste et al., 2014; Roulleau et al., 2015b), CSZ (Shangguan et al., 2000; Xu et al., 2004; Zhao et al., 2011, 2012; Cheng et al., 2014) and CCZ (Yokoyama et al., 1999; Hoke et al., 2000; Zhao et al., 2002; Walia et al., 2005; Newell et al., 2008; Klemperer et al., 2013; Zhang et al., 2014). (b) Comparison of Nd-Sr isotopes between mantle-derived magmas from MOR (Zindler and Hart, 1986), OSZ (GEOROC database), CSZ (Wang et al., 2006; Zou et al., 2014; Guo et al., 2015a) and CCZ (Guo et al., 2013, 2015b). Abbreviations: MOR, mid-ocean ridge; OSZ, oceanic subduction zone; CSZ, continental subduction zone; CCZ, continental collision zone.

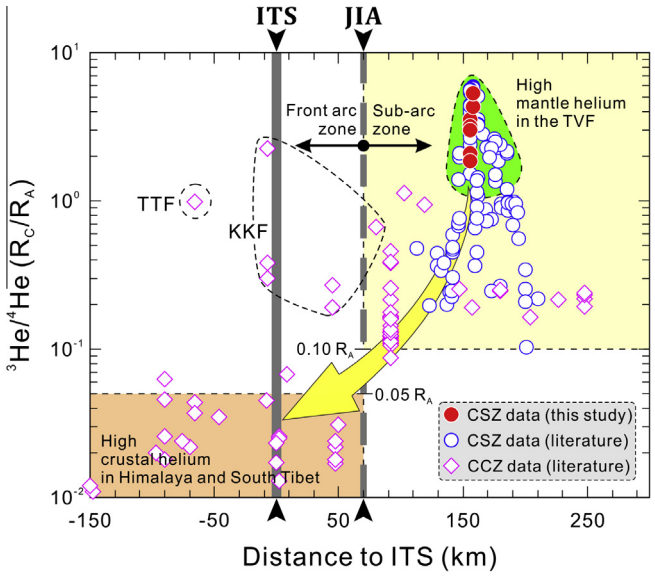

Fig. 11. Spatial variations in helium isotopes of volatiles from continental subduction zone (CSZ) and continental collision zone (CCZ). Data sources are as in Fig. 10. Abbreviations: ITS, Indus-Tsangpo suture; JIA, junction between Indian and Asian plates; TVF, Tengchong volcanic field; KKF, Karakoram fault; TTF, Tangra yumco-Tingri fault.

and (3) contamination by crustal radiogenic ^{4}He en route to the atmosphere.

Following reference ^{3}He/^{4}He range for arc-related volatiles (7.4 ± 1.3 R_A; Sano and Fischer, 2013), higher ^{3}He/^{4}He ratios (>6.1 R_A) are more likely to reflect nature of the EMW, while lower ^{3}He/^{4}He ratios (<6.1 R_A) commonly result from additional radiogenic ^{4}He contribution from overlying crust (Ray et al., 2009; M. Zhang et al., 2015). None of the TVF samples have ^{3}He/^{4}He ratios higher than 6.1 R_A (Fig. 10b), in stark contrast to typical OSZ samples. Additionally, ^{3}He/^{4}He ratios of the TVF samples are clearly higher than those of volatiles from CCZ (Fig. 10c; Yokoyama et al., 1999; Hoke et al., 2000; Zhao et al., 2002; Walia et al., 2005; Newell et al., 2008; Klemperer et al., 2013; Zhang et al., 2014). Negatively correlated Nd-Sr isotopes of mantle-derived magmas also indicate increasing degrees of mantle wedge enrichment from OSZ via CSZ to CCZ (Fig. 10d). Consequently, we can conclude that amount of recycled materials at CSZ is higher relative to that of OSZ, as indicated by systematic variations in He-Nd-Sr isotopes of mantle-derived magmas.

It is noted that low-R_A (<3 R_A) TVF samples partly overlap those from Himalaya and South Tibet (Fig. 11), suggesting that contribution from crustal radiogenic ^{4}He increases from CSZ to CCZ. The sub-arc zone exhibits high mantle helium emission as indicated by high ^{3}He/^{4}He ratios of volatiles from the TVF (Fig. 11). In contrast, samples from Himalaya and part of South Tibet (south of the JIA) are characterized by high crustal helium contribution, suggesting remarkable influence of accreted continental materials (i.e., accretionary plate margins; Sano and Fischer, 2013) in front arc zone. Additionally, high ^{3}He/^{4}He ratios of some samples from front arc zone can be attributed to dominant control of deep faults, such as the Karakoram fault (KKF; Klemperer et al., 2013). Therefore, we suggest that spatial variations in ^{3}He/^{4}He ratios for volatiles released from CSZ and CCZ can shed light on crust-mantle structure of the India-Asia continental subduction zone (Fig. 11).

6. Concluding remarks

Soil microseepage survey following accumulation chamber method reveals an average soil CO_2 flux of ca. 280 g m^{-2} d^{-1} and a total soil CO_2 output of 6.30 × 10^5 t a^{-1} for the RGP and adjacent region in the TVF, suggesting high carbon flux released by active volcanism at the India-Asia continental subduction zone. Based on available data, we conclude that total outgassing CO_2 flux of the whole TVF is about (4.48–7.05) × 10^6 t a^{-1}, which will add new data to global subaerial volcanic CO_2 flux. We propose that CO_2-rich volatiles released by modern hydrothermal activities (e.g., soil microseepage and hot springs) in the TVF can be attributed to continuous degassing of seismically-detected residual melts in upper crust. Eastward subduction of the Indian continental lithosphere provides recycled crustal materials for generation of enriched mantle wedge, which is considered as source region of the TVF parental magmas. As indicated by He-C isotope coupling model, contamination by crustal limestone can be the first-order control on He-CO_2 systematics of the TVF hydrothermal volatiles. The EMW-derived melts contribute about 45–85% of the total carbon inventory with the rest carbon (about 15–55%) accounted by crustal limestone. Mantle-derived magmas at continental subduction zone can be important triggers for liberation of carbon stored in carbonate rocks in overlying continental crust. He-Nd-Sr isotopes of magmas and volatiles from different types of plate boundaries highlight the distinctive volatile recycling model at continental subduction zone.

Acknowledgements

This study was financially supported by the National Natural Science Foundation of China (Grant No. 41572321), the Strategic Priority Research Program (B) of Chinese Academy of Sciences (Grant No. XDB03010600), and a project of the Chinese Ministry of Science and Technology (Sinoprobe-05-03). Leilei Ding, Yixuan Huang and Dengbu Yang are acknowledged for kind help during fieldwork, and Zhongping Li, Liwu Li, Li Du, Xiangxian Ma, Chunhui Cao and Xibin Wang for analyses of gas compositions and He-C isotopes.

Appendix A. Supplementary material

Supplementary data associated with this article can be found, in the online version, at http://dx.doi.org/10.1016/j.jseaes.2016.06.009.

References

Barry, P.H., Hilton, D.R., Fischer, T.P., de Moor, J.M., Mangasini, F., Ramirez, C., 2013. Helium and carbon isotope systematics of cold "mazuku" CO_2 vents and hydrothermal gases and fluids from Rungwe Volcanic Province, southern Tanzania. Chem. Geol. 339, 141–156.
Bebout, G.E., 1995. The impact of subduction-zone metamorphism on mantle-ocean chemical cycling. Chem. Geol. 126, 191–218.
Bouilhol, P., Jagoutz, O., Hanchar, J.M., Dudas, F.O., 2013. Dating the India-Eurasia collision through arc magmatic records. Earth Planet. Sci. Lett. 366, 163–175.
Burley, J.M.A., Katz, R.F., 2015. Variations in mid-ocean ridge CO_2 emissions driven by glacial cycles. Earth Planet. Sci. Lett. 426, 246–258.
Burton, M.R., Sawyer, G.M., Granieri, D., 2013. Deep carbon emissions from volcanoes. Rev. Mineral. Geochem. 75, 323–354.
Capitanio, F.A., Replumaz, A., 2013. Subduction and slab breakoff controls on Asian indentation tectonics and Himalayan western syntaxis formation. Geochem. Geophys. Geosyst. 14, 3515–3531.
Carapezza, M.L., Federico, C., 2000. The contribution of fluid geochemistry to the volcano monitoring of Stromboli. J. Volcanol. Geoth. Res. 95, 227–245.
Cheng, Z., Guo, Z., Zhang, M., Zhang, L., 2012. CO_2 flux estimations of hot springs in the Tengchong Cenozoic volcanic field, Yunnan Province, SW China. Acta Petrol. Sin. 28, 1217–1224 (in Chinese with English abstract).
Cheng, Z., Guo, Z., Zhang, M., Zhang, L., 2014. Carbon dioxide emissions from Tengchong Cenozoic volcanic field, Yunnan Province, SW China. Acta Petrol. Sin. 30, 3657–3670 (in Chinese with English abstract).
Chiodini, G., Cioni, R., Guidi, M., Raco, B., Marini, L., 1998. Soil CO_2 flux measurements in volcanic and geothermal areas. Appl. Geochem. 13, 543–552.
Clarke, W.B., Jenkins, W.J., Top, Z., 1976. Determination of Trinium by mass spectrometric measurement of ^{3}He. Int. J. Appl. Radiat. Isot. 27, 515–522.

Clift, P.D., Hodges, K.V., Heslop, D., Hannigan, R., Van Long, H., Calves, G., 2008. Correlation of Himalayan exhumation rates and Asian monsoon intensity. Nat. Geosci. 1, 875–880.
Cook-Kollars, J., Bebout, G.E., Collins, N.C., Angiboust, S., Agard, P., 2014. Subduction zone metamorphic pathway for deep carbon cycling: I. Evidence from HP/UHP metasedimentary rocks, Italian Alps. Chem. Geol. 386, 31–48.
Craig, H., Lupton, J., Horibe, Y., 1978. A mantle helium component in circum-Pacific volcanic gases: Hakone, the Marianas, and Mt. Lassen. In: Alexander, E.C., Ozima, M. (Eds.), Advances in Earth and Planetary Science Terrestrial Rare Gases. Academic publication, Japan, pp. 3–16.
D'Alessandro, W., Giammanco, S., Parello, F., Valenza, M., 1997. CO_2 output and $\delta^{13}C$ (CO_2) from Mount Etna as indicators of degassing of shallow asthenosphere. Bull. Volcanol. 58, 455–458.
DeCelles, P.G., Kapp, P., Quade, J., Gehrels, G.E., 2011. Oligocene-Miocene Kailas basin, southwestern Tibet: record of postcollisional upper-plate extension in the Indus-Yarlung suture zone. Geol. Soc. Am. Bull. 123, 1337–1362.
Ding, H., Zhang, Z., Dong, X., Tian, Z., Xiang, H., Mu, H., Gou, Z., Shui, X., Li, W., Mao, L., 2016. Early Eocene (c. 50 Ma) collision of the Indian and Asian continents: constraints from the North Himalayan metamorphic rocks, southeastern Tibet. Earth Planet. Sci. Lett. 435, 64–73.
Dixon, J.E., 1997. Degassing of alkalic basalts. Am. Mineral. 82, 368–378.
Dosseto, A., Vigier, N., Joannes-Boyau, R., Moffat, I., Singh, T., Srivastava, P., 2015. Rapid response of silicate weathering rates to climate change in the Himalaya. Geochem. Perspect. Lett. 1, 10–19.
Du, J., Liu, C., Fu, B., Ninomiya, Y., Zhang, Y., Wang, C., Wang, H., Sun, Z., 2005. Variations of geothermometry and chemical-isotopic compositions of hot spring fluids in the Rehai geothermal field, southwestern China. J. Volcanol. Geoth. Res. 142, 243–261.
Dupont-Nivet, G., Krijgsman, W., Langereis, C.G., Abels, H.A., Dai, S., Fang, X., 2007. Tibetan plateau aridification linked to global cooling at the Eocene-Oligocene transition. Nature 445, 635–638.
Evans, W.C., Bergfeld, D., McGimsey, R.G., Hunt, A.G., 2009. Diffuse gas emissions at the Ukinrek Maars, Alaska: implications for magmatic degassing and volcanic monitoring. Appl. Geochem. 24, 527–535.
Fielding, E., Isacks, B., Barazangi, M., Duncan, C., 1994. How flat is Tibet? Geology 22, 163–167.
Gao, J.-F., Zhou, M.-F., Robinson, P.T., Wang, C.Y., Zhao, J.-H., Malpas, J., 2015. Magma mixing recorded by Sr isotopes of plagioclase from dacites of the Quaternary Tengchong volcanic field, SE Tibetan Plateau. J. Asian Earth Sci. 98, 1–17.
Gautheron, C., Moreira, M., 2002. Helium signature of the subcontinental lithospheric mantle. Earth Planet. Sci. Lett. 199, 39–47.
Giggenbach, W.F., 1996. Chemical composition of volcanic gases. In: Scarpa, M., Tilling, R.J. (Eds.), Monitoring and Mitigation of Volcano Hazards. Springer-Verlag, Berlin Heidelberg, pp. 221–256.
Giggenbach, W.F., Poreda, R.J., 1993. Helium isotopic and chemical composition of gases from volcanic-hydrothermal systems in the Philippines. Geothermics 22, 369–380.
Graham, D.W., 2002. Noble gas isotope geochemistry of mid-ocean ridge and ocean island basalts: characterization of mantle source reservoirs. Rev. Mineral. Geochem. 47, 247–319.
Guo, Q., Wang, Y., 2012. Geochemistry of hot springs in the Tengchong hydrothermal areas, Southwestern China. J. Volcanol. Geoth. Res. 215–216, 61–73.
Guo, Z., Cheng, Z., Zhang, M., Zhang, L., Li, X., Liu, J., 2015a. Post-collisional high-K calc-alkaline volcanism in Tengchong volcanic field, SE Tibet: constraints on Indian eastward subduction and slab detachment. J. Geol. Soc. 172, 624–640.
Guo, Z., Wilson, M., Zhang, M., Cheng, Z., Zhang, L., 2015b. Post-collisional ultrapotassic mafic magmatism in South Tibet: products of partial melting of pyroxenite in the mantle wedge induced by roll-back and delamination of the subducted Indian continental lithosphere slab. J. Petrol. 56, 1365–1406.
Guo, Z., Ruddiman, W.F., Hao, Q., Wu, H., Qiao, Y., Zhu, R.X., Peng, S., Wei, J., Yuan, B., Liu, T., 2002. Onset of Asian desertification by 22 Myr ago inferred from loess deposits in China. Nature 416, 159–163.
Guo, Z., Wilson, M., Liu, J., 2007. Post-collisional adakites in south Tibet: products of partial melting of subduction-modified lower crust. Lithos 96, 205–224.
Guo, Z., Wilson, M., Liu, J., Mao, Q., 2006. Post-collisional, potassic and ultrapotassic magmatism of the northern Tibetan Plateau: constraints on characteristics of the mantle source, geodynamic setting and uplift mechanisms. J. Petrol. 47, 1177–1220.
Guo, Z., Wilson, M., Zhang, L., Zhang, M., Cheng, Z., Liu, J., 2014a. The role of subduction channel mélanges and convergent subduction systems in the petrogenesis of post-collisional K-rich mafic magmatism in NW Tibet. Lithos 198–199, 184–201.
Guo, Z., Zhang, M., Cheng, Z., Zhang, L., Liu, J., 2014b. Fluxes and genesis of greenhouse gases emissions from typical volcanic fields in China. Acta Petrol. Sin. 30, 3467–3480 (in Chinese with English abstract).
Guo, Z., Wilson, M., Zhang, M., Cheng, Z., Zhang, L., 2013. Post-collisional, K-rich mafic magmatism in south Tibet: constraints on Indian slab-to-wedge transport processes and plateau uplift. Contrib. Miner. Petrol. 165, 1311–1340.
Hahm, D., Hilton, D.R., Cho, M., Wei, H., Kim, K.R., 2008. Geothermal He and CO_2 variations at Changbaishan intra-plate volcano (NE China) and the nature of the sub-continental lithospheric mantle. Geophys. Res. Lett. 35, L22304.
Halldórsson, S.A., Hilton, D.R., Troll, V.R., Fischer, T.P., 2013. Resolving volatile sources along the western Sunda arc, Indonesia. Chem. Geol. 339, 263–282.
Hernández, P.A., Notsu, K., Tsurumi, M., Mori, T., Ohno, M., Shimoike, Y., Salazar, J., Pérez, N., 2003. Carbon dioxide emissions from soils at Hakkoda, north Japan. J. Geophys. Res. 108, 2210.
Hilton, D.R., 1996. The helium and carbon isotope systematics of a continental geothermal system: results from monitoring studies at Long Valley caldera (California, U.S.A.). Chem. Geol. 127, 269–295.
Hilton, D.R., Fischer, T.P., Marty, B., 2002. Noble gases and volatile recycling at subduction zones. Rev. Mineral. Geochem. 47, 319–370.
Hilton, D.R., Hammerschmidt, K., Teufel, S., Friedrichsen, H., 1993. Helium isotope characteristics of Andean geothermal fluids and lavas. Earth Planet. Sci. Lett. 120, 265–282.
Hilton, D.R., McMurtry, G.M., Goff, F., 1998. Large variations in vent fluid $CO_2/^3He$ ratios signal rapid changes in magma chemistry at Loihi seamount, Hawaii. Nature 396, 359–362.
Hoefs, J., 2009. Stable Isotope Geochemistry. Springer-Verlag, Berlin.
Hoke, L., Lamb, S., Hilton, D.R., Poreda, R.J., 2000. Southern limit of mantle-derived geothermal helium emissions in Tibet: implications for lithospheric structure. Earth Planet. Sci. Lett. 180, 297–308.
Huang, J., Zhao, D., 2006. High-resolution mantle tomography of China and surrounding regions. J. Geophys. Res. 111, B09305.
Huangfu, G., Jiang, C., 2000. Study on Tengchong Volcanic Activity. Science and Technology Publishing House of Yunnan, Kunming (in Chinese).
Iacono-Marziano, G., Paonita, A., Rizzo, A., Scaillet, B., Gaillard, F., 2010. Noble gas solubilities in silicate melts: new experimental results and a comprehensive model of the effects of liquid composition, temperature and pressure. Chem. Geol. 279, 145–157.
Inguaggiato, S., Mazot, A., Diliberto, I.S., Inguaggiato, C., Madonia, P., Rouwet, D., Vita, F., 2012. Total CO_2 output from Vulcano Island (Aeolian Islands, Italy). Geochem. Geophys. Geosyst. 13, Q02012.
Javoy, M., Pineau, F., Iiyama, I., 1978. Experimental determination of the isotopic fractionation between gaseous CO_2 and carbon dissolved in tholeiitic magma. Contrib. Miner. Petrol. 67, 35–39.
Jean-Baptiste, P., Allard, P., Fourré, E., Parello, F., Aiuppa, A., 2014. Helium isotope systematics of volcanic gases and thermal waters of Guadeloupe Island, Lesser Antilles. J. Volcanol. Geoth. Res. 283, 66–72.
Kagoshima, T., Sano, Y., Takahata, N., Maruoka, T., Fischer, T.P., Hattori, K., 2015. Sulphur geodynamic cycle. Sci. Reports 5, 8330.
Kelemen, P.B., Manning, C.E., 2015. Reevaluating carbon fluxes in subduction zones, what goes down, mostly comes up. Proc. Natl. Acad. Sci. 112, E3997–E4006.
Kerrick, D., Connolly, J., 2001. Metamorphic devolatilization of subducted marine sediments and the transport of volatiles into the Earth's mantle. Nature 411, 293–296.
Kerrick, D.M., Caldeira, K., 1999. Was the Himalayan orogen a climatically significant coupled source and sink for atmospheric CO_2 during the Cenozoic? Earth Planet. Sci. Lett. 173, 195–203.
Klemperer, S.L., Kennedy, B.M., Sastry, S.R., Makovsky, Y., Harinarayana, T., Leech, M. L., 2013. Mantle fluids in the Karakoram fault: helium isotope evidence. Earth Planet. Sci. Lett. 366, 59–70.
Lan, T.F., Yang, T.F., Lee, H.F., Chen, Y.G., Chen, C.H., Song, S.R., Tsao, S., 2007. Compositions and flux of soil gas in Liu-Huang-Ku hydrothermal area, northern Taiwan. J. Volcanol. Geoth. Res. 165, 32–45.
Lee, C.-T.A., Lackey, J.S., 2015. Global continental arc flare-ups and their relation to long-term greenhouse conditions. Elements 11, 125–130.
Lee, C.-T.A., Shen, B., Slotnick, B.S., Liao, K., Dickens, G.R., Yokoyama, Y., Lenardic, A., Dasgupta, R., Jellinek, M., Lackey, J.S., Schneider, T., Tice, M.M., 2013. Continental arc-island arc fluctuations, growth of crustal carbonates, and long-term climate change. Geosphere 9, 21–36.
Lei, J., Xie, F., Fan, Q., Santosh, M., 2013. Seismic imaging of the deep structure under the Chinese volcanoes: an overview. Phys. Earth Planet. Inter. 224, 104–123.
Lei, J., Zhao, D., 2016. Teleseismic P-wave tomography and mantle dynamics beneath Eastern Tibet. Geochem. Geophys. Geosyst. http://dx.doi.org/10.1002/2016GC006262.
Li, Z., Wang, X., Li, L., Zhang, M., Tao, M., Xing, L., Cao, C., Xia, Y., 2014. Development of new method of $\delta^{13}C$ measurement for trace hydrocarbons in natural gas using solid phase micro-extraction coupled to gas chromatography isotope ratio mass spectrometry. J. Chromatogr. A 1372, 228–235.
Lowenstern, J.B., Bergfeld, D., Evans, W.C., Hunt, A.G., 2015. Origins of geothermal gases at Yellowstone. J. Volcanol. Geoth. Res. 302, 87–101.
Luo, M., Huang, H., Zhang, P., Wu, Q., Chen, D., 2014. Origins of gas discharging from the Qiangtang Basin in the northern Qinghai-Tibet Plateau, China: evidence from gas compositions, helium, and carbon isotopes. J. Geochem. Explor. 146, 119–126.
Lupton, J.E., 1983. Terrestrial inert gases isotope tracer studies and clues to primordial components in the mantle. Annu. Rev. Earth Planet. Sci. 11, 371–414.
Mamyrin, B.A., Anufriev, G.S., Kamenskii, I.L., Tolstikhin, I.N., 1970. Determination of the isotopic composition of atmospheric Helium. Geochem. Int. 7, 498–505.
Marty, B., Jambon, A., 1987. $C/^3He$ in volatile fluxes from the solid Earth: implications for carbon geodynamics. Earth Planet. Sci. Lett. 83, 16–26.
Marty, B., Jambon, A., Sano, Y., 1989. Helium isotopes and CO_2 in volcanic gases of Japan. Chem. Geol. 76, 25–40.
Mitchell, A.H.G., 1993. Cretaceous-Cenozoic tectonic events in the western Myanmar (Burma)-Assam region. J. Geol. Soc. 150, 1089–1102.
Mo, X., Niu, Y., Dong, G., Zhao, Z., Hou, Z., Zhou, S., Ke, S., 2008. Contribution of syncollisional felsic magmatism to continental crust growth: a case study of the Paleogene Linzizong volcanic Succession in southern Tibet. Chem. Geol. 250, 49–67.
Moreira, M., 2013. Noble gas constraints on the origin and evolution of Earth's volatiles. Geochem. Perspect. 2, 229–230.

Najman, Y., Appel, E., Boudagher-Fadel, M., Bown, P., Carter, A., Garzanti, E., Godin, L., Han, J., Liebke, U., Oliver, G., 2010. Timing of India-Asia collision: geological, biostratigraphic, and palaeomagnetic constraints. J. Geophys. Res. 115, B12416.
Newell, D.L., Jessup, M.J., Cottle, J.M., Hilton, D.R., Sharp, Z.D., Fischer, T.P., 2008. Aqueous and isotope geochemistry of mineral springs along the southern margin of the Tibetan plateau: implications for fluid sources and regional degassing of CO_2. Geochem. Geophys. Geosyst. 9, Q08014.
Niu, Y., Zhao, Z., Zhu, D.-C., Mo, X., 2013. Continental collision zones are primary sites for net continental crust growth—a testable hypothesis. Earth Sci. Rev. 127, 96–110.
Notsu, K., Sugiyama, K., Hosoe, M., Uemura, A., Shimoike, Y., Tsunomori, F., Sumino, H., Yamamoto, J., Mori, T., Hernández, P.A., 2005. Diffuse CO_2 efflux from Iwojima volcano, Izu-Ogasawara arc, Japan. J. Volcanol. Geoth. Res. 139, 147–161.
O'Nions, R.K., Oxburgh, E.R., 1988. Helium, volatile fluxes and the development of continental crust. Earth Planet. Sci. Lett. 90, 331–347.
Ozima, M., Podosek, F.A., 1983. Noble Gas Geochemistry. Cambridge University Press, Cambridge.
Pineau, F., Javoy, M., 1983. Carbon isotopes and concentrations in mid-oceanic ridge basalts. Earth Planet. Sci. Lett. 62, 239–257.
Poli, S., Franzolin, E., Fumagalli, P., Crottini, A., 2009. The transport of carbon and hydrogen in subducted oceanic crust: an experimental study to 5 GPa. Earth Planet. Sci. Lett. 278, 350–360.
Ramaswamy, V., Gaye, B., Shirodkar, P.V., Rao, P.S., Chivas, A.R., Wheeler, D., Thwin, S., 2008. Distribution and sources of organic carbon, nitrogen and their isotopic signatures in sediments from the Ayeyarwady (Irrawaddy) continental shelf, northern Andaman Sea. Mar. Chem. 111, 137–150.
Ray, M.C., Hilton, D.R., Muñoz, J., Fischer, T.P., Shaw, A.M., 2009. The effects of volatile recycling, degassing and crustal contamination on the helium and carbon geochemistry of hydrothermal fluids from the Southern Volcanic Zone of Chile. Chem. Geol. 266, 38–49.
Raymo, M., Ruddiman, W.F., 1992. Tectonic forcing of late Cenozoic climate. Nature 359, 117–122.
Rison, W., Craig, H., 1983. Helium isotopes and mantle volatiles in Loihi Seamount and Hawaiian Island basalts and xenoliths. Earth Planet. Sci. Lett. 66, 407–426.
Roulleau, E., Sano, Y., Takahata, N., Yang, F.T., Takahashi, H.A., 2015a. He, Ar, N and C isotope compositions in Tatun Volcanic Group (TVG), Taiwan: evidence for an important contribution of pelagic carbonates in the magmatic source. J. Volcanol. Geoth. Res. 303, 7–15.
Roulleau, E., Vinet, N., Sano, Y., Takahata, N., Shinohara, H., Ooki, M., Takahashi, H.A., Furukawa, R., 2015b. Effect of the volcanic front migration on helium, nitrogen, argon, and carbon geochemistry of hydrothermal/magmatic fluids from Hokkaido volcanoes, Japan. Chem. Geol. 414, 42–58.
Sano, Y., Fischer, T.P., 2013. The analysis and interpretation of noble gases in modern hydrothermal systems. In: Burnard, P. (Ed.), The Noble Gases as Geochemical Tracers. Springer-verlag, Berlin Heidelberg, pp. 249–317.
Sano, Y., Hirabayashi, J.-I., Oba, T., Gamo, T., 1994. Carbon and helium isotopic ratios at Kusatsu-Shirane Volcano, Japan. Appl. Geochem. 9, 371–377.
Sano, Y., Marty, B., 1995. Origin of carbon in fumarolic gas from island arcs. Chem. Geol. 119, 265–274.
Sano, Y., Nakajima, J., 2008. Geographical distribution of $^3He/^4He$ ratios and seismic tomography in Japan. Geochem. J. 42, 51–60.
Sano, Y., Nishio, Y., Sasaki, S., Gamo, T., Nagao, K., 1998. Helium and carbon isotope systematics at Ontake volcano, Japan. J. Geophys. Res. 103, 23863–23873.
Sano, Y., Takahata, N., Nishio, Y., Fischer, T.P., Williams, S.N., 2001. Volcanic flux of nitrogen from the Earth. Chem. Geol. 171, 263–271.
Sano, Y., Takahata, N., Seno, T., 2006. Geographical distribution of $^3He/^4He$ ratios in the Chugoku District, southwestern Japan. Pure Appl. Geophys. 163, 745–757.
Sano, Y., Williams, S.N., 1996. Fluxes of mantle and subducted carbon along convergent plate boundaries. Geophys. Res. Lett. 23, 2749–2752.
Shangguan, Z., Bai, C., Sun, M., 2000. Mantle-derived magmatic gas releasing features at the Rehai area, Tengchong County, Yunnan Province, China. Sci. China (Series D) 43, 132–140.
Shangguan, Z., Gao, Q., Zhao, C., 2004. Geochemical evidence of the activity of the NW-trending fault at Rehai area, Tengchong, Yunnan Province, China. Seismol. Geol. 26, 46–51 (in Chinese with English abstract).
Shangguan, Z., Zhao, C., Li, H., Gao, Q., Sun, M., 2005. Evolution of hydrothermal explosions at Rehai geothermal field, Tengchong volcanic region, China. Geothermics 34, 518–526.
Shaw, A.M., Hilton, D.R., Fischer, T.P., Walker, J.A., Alvarado, G.E., 2003. Contrasting He–C relationships in Nicaragua and Costa Rica: insights into C cycling through subduction zones. Earth Planet. Sci. Lett. 214, 499–513.
Shi, D., Wu, Z., Klemperer, S.L., Zhao, W., Xue, G., Su, H., 2015. Receiver function imaging of crustal suture, steep subduction, and mantle wedge in the eastern India-Tibet continental collision zone. Earth Planet. Sci. Lett. 414, 6–15.
Shields, G., Veizer, J., 2002. Precambrian marine carbonate isotope database: Version 1.1. Geochem. Geophys. Geosyst. 3. http://dx.doi.org/10.1029/2001GC000266.
Sinclair, A.J., 1974. Selection of threshold values in geochemical data using probability graphs. J. Geochem. Explor. 3, 129–149.
Stagno, V., Ojwang, D.O., McCammon, C.A., Frost, D.J., 2013. The oxidation state of the mantle and the extraction of carbon from Earth's interior. Nature 493, 84–88.
Staudacher, T., Allègre, C.J., 1988. Recycling of oceanic crust and sediments: the noble gas subduction barrier. Earth Planet. Sci. Lett. 89, 173–183.
Sverjensky, D.A., Stagno, V., Huang, F., 2014. Important role for organic carbon in subduction-zone fluids in the deep carbon cycle. Nat. Geosci. 7, 909–913.
Tapponnier, P., Xu, Z., Roger, F., Meyer, B., Arnaud, N., Wittlinger, G., Yang, J., 2001. Oblique stepwise rise and growth of the Tibet Plateau. Science 294, 1671–1677.
Taran, Y.A., 2009. Geochemistry of volcanic and hydrothermal fluids and volatile budget of the Kamchatka-Kuril subduction zone. Geochim. Cosmochim. Acta 73, 1067–1094.
Taran, Y., 2011. N_2, Ar, and He as a tool for discriminating sources of volcanic fluids with application to Vulcano, Italy. Bull. Volcanol. 73, 395–408.
Torgersen, T., Jenkins, W.J., 1982. Helium isotopes in geothermal systems: Iceland, The Geysers, Raft River and Steamboat Springs. Geochim. Cosmochim. Acta 46, 739–748.
Van Soest, M.C., Hilton, D.R., Kreulen, R., 1998. Tracing crustal and slab contributions to arc magmatism in the Lesser Antilles island arc using helium and carbon relationships in geothermal fluids. Geochim. Cosmochim. Acta 62, 3323–3335.
Varekamp, J.C., Kreulen, R., Poorte, R.P.E., Van Bergen, M.J., 1992. Carbon sources in arc volcanism, with implications for the carbon cycle. Terra Nova 4, 363–373.
Walia, V., Quattrocchi, F., Virk, H.S., Yang, T.F., Pizzino, L., Bajwa, B.S., 2005. Radon, helium and uranium survey in some thermal springs located in NW Himalayas, India: mobilization by tectonic features or by geochemical barriers? J. Environ. Monit. 7, 850–855.
Wang, C., Dai, J., Zhao, X., Li, Y., Graham, S.A., He, D., Ran, B., Meng, J., 2014. Outward-growth of the Tibetan Plateau during the Cenozoic: a review. Tectonophysics 621, 1–43.
Wang, F., Peng, Z., Chen, W., Wang, Z., Yang, J., Zhang, Z., Hu, Y., 2000. High-precision thermal ionization mass spectrometry dating of young volcanic rocks by using U-series method. Chin. Sci. Bull. 45, 83–87.
Wang, F., Peng, Z., Zhu, R., He, H., Yang, L., 2006. Petrogenesis and magma residence time of lavas from Tengchong volcanic field (China): evidence from U series disequilibria and $^{40}Ar/^{39}Ar$ dating. Geochem. Geophys. Geosyst. 7, Q01002.
Wang, G., Wan, J., Wang, E., Zheng, D., Li, F., 2008. Late Cenozoic to recent transtensional deformation across the Southern part of the Gaoligong shear zone between the Indian plate and SE margin of the Tibetan plateau and its tectonic origin. Tectonophysics 460, 1–20.
Weiss, R.F., 1971. Solubility of helium and neon in water and seawater. J. Chem. Eng. Data 16, 235–241.
Werner, C., Brantley, S., 2003. CO_2 emissions from the Yellowstone volcanic system. Geochem. Geophys. Geosyst. 4, 1061.
Willenbring, J.K., Codilean, A.T., McElroy, B., 2013. Earth is (mostly) flat: apportionment of the flux of continental sediment over millennial time scales. Geology 41, 343–346.
Wu, G., Liu, Y., He, B., Bao, Q., Duan, A., Jin, F.-F., 2012. Thermal controls on the Asian summer monsoon. Sci. Reports 2, 404.
Xu, S., Nakai, S.i., Wakita, H., Wang, X., 2004. Carbon and noble gas isotopes in the Tengchong volcanic geothermal area, Yunnan, southwestern China. Acta Geol. Sin. (English Edition) 78, 1122–1135.
Xu, Y., Yang, X., Li, Z., Liu, J., 2012. Seismic structure of the Tengchong volcanic area southwest China from local earthquake tomography. J. Volcanol. Geoth. Res. 239–240, 83–91.
Xu, Z., Wang, Q., Cai, Z., Dong, H., Li, H., Chen, X., Duan, X., Cao, H., Li, J., Burg, J.-P., 2015. Kinematics of the Tengchong Terrane in SE Tibet from the late Eocene to early Miocene: insights from coeval mid-crustal detachments and strike-slip shear zones. Tectonophysics 665, 127–148.
Yang, H., Hu, J., Hu, Y., Duan, Y., Li, G., 2013. Crustal structure in the Tengchong volcanic area and position of the magma chambers. J. Asian Earth Sci. 73, 48–56.
Yang, T.F., Lan, T.F., Lee, H.F., Fu, C.C., Chuang, P.C., Lo, C.H., Chen, C.H., Chen, C.A., Lee, C.S., 2005. Gas compositions and helium isotopic ratios of fluid samples around Kueishantao, NE offshore Taiwan and its tectonic implications. Geochem. J. 39, 469–480.
Yokoyama, T., Nakai, S., Wakita, H., 1999. Helium and carbon isotopic compositions of hot spring gases in the Tibetan Plateau. J. Volcanol. Geoth. Res. 88, 99–107.
Zellmer, G.F., Edmonds, M., Straub, S.M., 2015. Volatiles in subduction zone magmatism. Geol. Soc., London, Special Publ. 410, 1–17.
Zhang, L., Guo, Z., Zhang, M., Cheng, Z., 2014. Study on soil micro-seepage gas flux in the high temperature geothermal area: an example from the Yangbajing geothermal field, South Tibet. Acta Petrol. Sin. 30, 3612–3626 (in Chinese with English abstract).
Zhang, L., Guo, Z., Zhang, M., Cheng, Z., Sun, Y., 2015. Post-collisional potassic magmatism in the eastern Lhasa terrane, south Tibet: products of partial melting of mélanges in a continental subduction channel. Gondwana Res. http://dx.doi.org/10.1016/j.gr.2015.11.007.
Zhang, M., Guo, Z., Cheng, Z., Zhang, L., Guo, W., Yang, C., Fu, Q., Wen, X., 2011. Greenhouse gases flux estimation of hot springs in Changbaishan volcanic field, NE China. Acta Petrol. Sin. 27, 2898–2904 (in Chinese with English abstract).
Zhang, M., Guo, Z., Sano, Y., Cheng, Z., Zhang, L., 2015. Stagnant subducted Pacific slab-derived CO_2 emissions: insights into magma degassing at Changbaishan volcano, NE China. J. Asian Earth Sci. 106, 49–63.
Zhang, Y.Z., Zhang, D.H., Liu, S.-R., 1996. Stratigraphy (Lithostratic) of Yunnan Province. China University of Geosciences Press, Wuhan.
Zhao, C., Ran, H., Chen, K., 2011. Present-day temperatures of magma chambers in the crust beneath Tengchong volcanic field, southeastern China: estimation from carbon isotopic fractionation between CO_2 and CH_4 of free gases escaped from thermal springs. Acta Petrol. Sin. 27, 2883–2897 (in Chinese with English abstract).

Zhao, C., Ran, H., Wang, Y., 2012. Present-day mantle-derived helium release in the Tengchong volcanic field, Southeast China: implications for tectonics and magmatism. Acta Petrol. Sin. 28, 1189–1204 (in Chinese with English abstract).
Zhao, P., Xie, E., Dor, J., Jin, J., Hu, X., Du, S., Yao, Z., 2002. Geochemical characteristics of geothermal gases and their geological implications in Tibet. Acta Petrol. Sin. 18, 539–550 (in Chinese with English abstract).
Zheng, H., Wei, X., Tada, R., Clift, P.D., Wang, B., Jourdan, F., Wang, P., He, M., 2015. Late Oligocene–early Miocene birth of the Taklimakan Desert. Proc. Natl. Acad. Sci. 112, 7662–7667.
Zhou, M.-F., Robinson, P., Wang, C., Zhao, J.-H., Yan, D.-P., Gao, J.-F., Malpas, J., 2012. Heterogeneous mantle source and magma differentiation of quaternary arc-like volcanic rocks from Tengchong, SE margin of the Tibetan Plateau. Contrib. Miner. Petrol. 163, 841–860.
Zhu, B., Mao, C., Lugmair, G., Macdougall, J., 1983. Isotopic and geochemical evidence for the origin of Plio-Pleistocene volcanic rocks near the Indo-Eurasian collisional margin at Tengchong, China. Earth Planet. Sci. Lett. 65, 263–275.
Zhu, D.-C., Wang, Q., Zhao, Z.-D., Chung, S.-L., Cawood, P.A., Niu, Y., Liu, S.-A., Wu, F.-Y., Mo, X.-X., 2015. Magmatic record of India-Asia collision. Sci. Reports 5, 14289.
Zindler, A., Hart, S., 1986. Chemical geodynamics. Annu. Rev. Earth Planet. Sci. 14, 493–571.
Zou, H., Fan, Q., Schmitt, A.K., Sui, J., 2010. U–Th dating of zircons from Holocene potassic andesites (Maanshan volcano, Tengchong, SE Tibetan Plateau) by depth profiling: time scales and nature of magma storage. Lithos 118, 202–210.
Zou, H., Shen, C.-C., Fan, Q., Lin, K., 2014. U-series disequilibrium in young Tengchong volcanics: recycling of mature clay sediments or mudstones into the SE Tibetan mantle. Lithos 192–195, 132–141.